Icarus 364 (2021) 114471

Contents lists available at ScienceDirect

Icarus

journal homepage: www.elsevier.com/locate/icarus

Research Paper

Manganese oxides in Martian meteorites Northwest Africa (NWA) 7034 and 7533

Yang Liu [a,*], Woodward W. Fischer [b], Chi Ma [b], John R. Beckett [b], Oliver Tschauner [c], Yunbin Guan [b], Usha F. Lingappa [b], Samuel M. Webb [d], Vitali B. Prakapenka [e], Nina L. Lanza [f], Carl B. Agee [g]

[a] Jet Propulsion Laboratory, California Institute of Technology, Pasadena, CA 91109, USA
[b] Division of Geological and Planetary Sciences, California Institute of Technology, Pasadena, CA 91125, USA
[c] Department of Geoscience, University of Nevada, Las Vegas, NV 89154, USA
[d] Stanford Synchrotron Radiation Lightsource, Stanford University, Menlo Park, CA 94025, USA
[e] GSECARS, Argonne National Laboratory, Argonne, IL60439, USA
[f] Los Alamos National Laboratory, P.O. Box 1663, Los Alamos, NM 87545, USA
[g] Institute of Meteoritics, University of New Mexico, Albuquerque, NM 87131, USA

ARTICLE INFO

Keywords:
Mars
Oxygen
Mn-oxides
Atmosphere

ABSTRACT

We report the discovery of indigenous Mn-oxides in Martian regolith breccias Northwest Africa (NWA) 7034 and 7533. These Mn-oxides occur in Mn-rich regions as nanocrystals mixed with silicates, FeOOH, and possible phosphates. The Mn-rich regions contain up to 34 wt% Mn and typically display large chemical gradients on the scale of 10–20 μm. The Martian origin of Mn-oxides was established by the presence of Mn-rich glass (4.8–5.6 wt % Mn) in the fusion crust that crosscuts a Mn-oxides-bearing monzonite clast and by the absence of Mn-oxides on the environmentally exposed surfaces (exterior and fractures) of the meteorites. Manganese K-edge X-ray absorption spectrum (XAS) of the Mn-rich glass in the fusion crust indicated that this glass included high-valent Mn species. Synchrotron micro-X-ray diffraction of a Mn-rich region in a basalt clast and XAS of Mn-rich regions in three monzonite clasts indicate Mn-oxides in these regions are dominantly hollandite-structured with 67–85 mol % of the total Mn being Mn^{4+}. The fact that Mn-rich regions are present in diverse petrological associations but are absent in the matrix of the breccias indicates that the Mn-oxides formed through surface alteration prior to the final brecciation event that assembled NWA 7034 and 7533. Thus, the age of the Mn-oxides is older than the lithification age (arguably 1.35 Ga) of NWA 7034 and 7533. Together with findings of Mn-rich phases within Noachian and Hesperian sedimentary strata in Endeavour and Gale craters, our results suggest that Mn-oxides are a common weathering product on Mars, suggesting aqueous environment on the Martian surface with high redox potential.

1. Introduction

Manganese (3+, 4+)-(hydr)oxides are important indicators of environmental conditions because their formation from Mn^{2+} indicates an environment of high redox potential (Crerar et al., 1980). The Mn^{4+}/Mn^{2+} pair is also of interest to the study of astrobiology given that they are valuable electron acceptors for the anaerobic respiration of microbes (Tebo et al., 2004; Johnson et al., 2013; Johnson et al., 2016). Manganese is a minor element in rock-forming minerals so that deposits of Mn-oxides typically indicate processes to enrich Mn through weathering and alteration processes. Thermodynamics calculations show that Mn^{2+} in aqueous solutions (Mn^{2+}(aq)) is stable under a wide range of solution chemistry, pH, and redox conditions (Crerar et al., 1980; Noda et al., 2019). Together with the slow kinetics of oxidizing Mn^{2+}(aq) into insoluble Mn oxides (Morgan, 2005), enriching Mn in aqueous solutions to form significant quantities of $Mn^{4+,3+}$-oxides typically requires long-lasting aqueous environments. Importantly, oxidation of Mn^{2+}(aq) into insoluble MnO_2 or Mn_2O_3 occurs at high redox potentials (Eh > +0.5 V) for surface fluids of pH = 7 and a total Mn concentration of 1 μmol/L to 1 mmol/L total Mn (Crerar et al., 1980; Noda et al., 2019). For acidic

* Corresponding author.
E-mail address: Yang.Liu@jpl.nasa.gov (Y. Liu).

https://doi.org/10.1016/j.icarus.2021.114471
Received 7 January 2021; Received in revised form 19 February 2021; Accepted 6 April 2021
Available online 20 April 2021

solutions, an even higher redox potential is required (Eh > +0.8 V at pH = 6, Noda et al., 2019). The most readily high-Eh materials for Mn oxidation are dissolved O_2 species in aqueous solutions (atmospheric O_2 or its photochemical products).

Remote sensing and in situ measurements of Martian soils, sedimentary rocks, and rock surface coatings have observed abundant signs of oxidized forms of Fe (goethite, magnetite, hematite) and S as sulfate salts (e.g., jarosite, $KFe^{3+}{}_3(SO_4)_2(OH)_6$) in surface terrains (Morris et al., 2004; Haskin et al., 2005; Yen et al., 2005; Bibring et al., 2006; Morris et al., 2006; Hurowitz et al., 2010). These observations suggested that Martian surface is oxidizing. Recently, the Opportunity and Curiosity rovers encountered Mn-rich materials (19.4–26.8 wt% Mn) within Noachian and Hesperian strata at Endeavour crater and Gale crater, respectively, suggesting a stronger redox gradient in some near-surface environments than previously recognized (Lanza et al., 2014; Arvidson et al., 2016; Lanza et al., 2016; Meslin, 2018; Gasda et al., 2019). However, the redox state of Mn in these Mn-rich materials was not determined due to instrument limitations and the inference that these are high-valence Mn oxides could only be made indirectly on the basis of dark spectral properties and correlation of Mn with certain trace metals (Lanza et al., 2016).

Within Martian meteorites, Mn-oxides had not previously been reported until NWA 7034 and 7533 (Liu et al., 2017). NWA 7034 and 7533 are paired meteorites, deriving from the same meteor that entered Earth's atmosphere. Together with several other pieces, they belong to a newly recognized type of Martian meteorite, Martian regolith breccia, with unique minerals, rock fragments, and isotope geochemistry that shed new light on the surface and crustal processes of Mars (e.g., Agee et al., 2013; Humayun et al., 2013). The alkali-rich basalt and monzonite fragments found in these meteorites are not represented by other igneous Martian meteorites but are similar in alkali-silica contents and mineralogy to some igneous rocks measured by the Curiosity rover (Grotzinger, 2015; Santos et al., 2015; Sautter et al., 2016; Hewins et al., 2017). Crystallization ages of zircons in alkali-rock fragments suggest early crustal differentiation at >4.4 Ga (Humayun et al., 2013; McCubbin et al., 2016; Bouvier et al., 2018). Multiple lines of evidence suggest that these breccias likely experienced a single whole-rock thermal event that coincided with the lithification of the breccia, including the observation of similar ages between the disturbance in the U-Pb isotope systems in zircons and apatite (Humayun et al., 2013; Bellucci et al., 2015; McCubbin et al., 2016) and the annealed texture of the matrix (Leroux et al., 2016; McCubbin et al., 2016). This thermal event was also credited for the formation of Ni-rich pyrite (Lorand et al., 2015). Conversely, the stable isotopic signatures of NWA 7034 and 7533 suggested the involvement of surface materials that were previously exchanged with the Martian atmosphere or hydrosphere (Nemchin et al., 2014). The higher $\delta^{18}O$ and $\Delta^{17}O$ values ($\delta^{18}O > 5.5‰$ and $\Delta^{17}O > 0.55‰$) of rock chips, magnetic separates, and a plagioclase clast of NWA 7034 relative to pyroxene grains in NWA 7034 and igneous Martian meteorites ($\delta^{18}O$ = 3.5–5.5‰ and $\Delta^{17}O \sim 0.33‰$) indicate multiple oxygen sources and a significant role of surficial aqueous alteration in the formation of NWA 7034 (Agee et al., 2013; Ziegler et al., 2013). More importantly, zircon grains display intracrystal variations of $\delta^{18}O$ by 3‰ and variable $\Delta^{17}O$ values (0.46 ± 0.19‰ to 2.16 ± 0.56‰) over an age span from 4.4 Ga to 1.7 Ga, which are attributed to the incorporation of surface regolith in the melt that formed zircons and to the continuous interaction with surface and hydrosphere/atm since 4.43 Ga (Nemchin et al., 2014). Sulfur isotopic compositions of NWA 7533 sulfide grains show mass-independent fractionation ($\Delta^{33}S$ of −0.05 to −0.30‰) with $\delta^{34}S$ ranges from −1.5 to −3.1‰, confirming the involvement of recycled, photochemically-processed sulfur (Lorand et al., 2020). Furthermore, several lines of mineralogical and textural evidence show that components in NWA 7034 and 7533 experienced alteration events before they were enclosed in the breccias, including alteration veins confined only to impact clasts (McCubbin et al., 2016; Hewins et al., 2017), Ce-monazite-inclusions ($CePO_4$) in apatite (Liu et al., 2016), Ni-rich pyrite and pyrite veins (Lorand et al., 2020). Our preliminary report of Mn^{4+}-oxides in NWA 7034 and 7533 hinted that some of these alterations occurred at low-temperatures on Mars (Liu et al., 2017). Additional signs of low-temperature aqueous alterations in NWA 7475, a paired rock of NWA 7034 and 7533, include Ni-poor pyrite, magnetite, and maghemite as alteration products (Wittmann et al., 2015) and Amazonian aqueous alteration of zircons from U-Th-Pb (Guitreau and Flahaut, 2019).

Here, we present detailed mineralogical, textural, and geochemical studies of the Mn-rich materials first reported in Liu et al. (2017) and establish their Martian origin. Our results show that Mn-rich materials are mixtures (aggregates) of maghemite- and hollandite [$Ba(Mn^{4+}Mn^{2+})O_{16}$]-structured oxides, providing concrete support for the view that manganese oxides form on Mars (Lanza et al., 2016). Based on the petrological settings of these Mn-rich materials, we determined the relative timing of Mn-oxides in the assembly of NWA 7034 and pairs. The formation of Mn-oxides likely involved sustained fluid activities under oxidizing conditions.

2. Samples and methods

At Caltech/JPL we studied four polished sections each of NWA 7034 and NWA 7533 (section images in Figs. S1–S8). The petrography of the sections was examined by reflected and transmitted light microscopy using a Leica DM 4500 polarized microscope. In addition, we also collected Na *K*α, Cr *K*α, Mn *K*α, Ti *K*α, and Ba *L*α maps for all of the sections using wavelength dispersive spectroscopy (WDS) on a JXA-8200 electron probe micro-analyzer (EPMA) with a 15 kV, 150–200 nA, and 35 μm diameter electron beam. Intensity maps of Na *K*α and Mn *K*α aided the search for Mn-rich phases and those of Ti *K*α and Ba *L*α were used to check for correlations of Mn with Ti and Ba. This approach readily identified microscale regions with average Mn elemental abundances >5 wt%.

The textural association of Mn-phases was further examined using a ZEISS 1550VP Field Emission Scanning Electron Microscope (SEM). The compositions of different phases were determined using an Oxford X-Max SDD energy-dispersive X-ray spectrometer (EDS) with the XPP matrix correction procedure calibrated with internal standards. Electron back-scatter diffraction (EBSD) analysis was conducted on the uncoated Mn-rich phases using the ZEISS SEM with a focused electron beam of 20 kV and 6 nA, a 70° tilted stage and a variable pressure of 25 Pa. A single-crystal silicon standard was used to calibrate the EBSD system.

Precise compositions of Mn-rich regions were determined using EPMA with a 15 kV and 5–10 nA beam with a diameter of 1–5 μm over three sessions. In two analytical sessions, *K*α lines of Si, Ti, Fe, Mg, K, Mn, Ni, Zn, S, P, and Cl, and *L*α of Ba were counted for 20 s, Na for 40 s, and Al and Ca for 60 s. In another analytical session, we measured all of the above elements except for Cl and 20 s was used to collect all of the peak counts. The mean atomic number (MAN) method (Donovan and Tingle, 1996) was used for the background corrections. Standards for analysis include natural and synthetic materials. For Mn-minerals, we calculated elemental oxide compositions by assuming Mn to be 4+ and Fe to be 3+, then renormalizing the elemental weight percentages to a total of 100%. For silicates and apatite, elemental oxide compositions were calculated with Fe and Mn as 2 + .

Qualitative elemental maps of several Mn-rich regions were generated using Mg *K*α, Si *K*α, Fe *K*α, Mn *K*α, and Ba *L*α X-rays collected with EPMA WDS. A focused electron beam with a 15 kV voltage and a 30 nA current was used. Step sizes ranged from 0.3 μm to 2 μm depending on the size of the Mn-regions and the host clasts.

Due to the small size of the Mn-rich phases, we used synchrotron X-ray microprobe techniques with ~2 μm resolution to obtain X-ray absorption spectra (XAS) on small sample domains and constructed microscale "redox" maps in the regions of interest identified by electron microscopy on a polished section (NWA 7533 C2b). X-ray absorption near-edge spectroscopy (XANES) measurements were performed using

the Beam Line 2–3 at Stanford Synchrotron Radiation Lightsource (SSRL) using chemical imaging and spectroscopy procedures similar to those described in Johnson et al. (2016). Energy calibration for a session was accomplished by referencing intensities to the mid-point peak absorption of the conspicuous pre-edge of a potassium permanganate standard at 6543.43 eV. Regions of interest were mapped in high resolution with a 2 μm beam using Kirkpatrick Baez mirrors for focusing. The X-ray fluorescence signals were collected using a Vortex SII International Silicon drift detector equipped with Quantum Detectors Xspress3 electronics for pulse processing at each 5 μm × 5 μm pixel. We collected full XANES spectra for end-member phases within the samples. We imaged two types of occurrences using redox distinctive energies determined from examining the normalized fluorescence differences relative to these endmembers. The redox-distinguishing energies chosen for high-resolution maps of Mn were 6553, 6558, 6561, 6573, and 6640 eV (Johnson et al., 2016). We reduced these multiple energy maps using the MicroAnalysis Toolkit software (Webb, 2011) with a non-negative linear–least squares fit of the data for each pixel to the end-member spectra, a Mn^{2+}-bearing silicate (rhodonite, $MnSiO_3$, from Butte County, CA, Caltech collection), and a Mn^{4+}-oxide. Confirmation of the fit was observed by examining XANES spectra at pixels identified as distinct by a principal component analysis of the multiple energies. To estimate the relative amounts of Mn^{3+} and Mn^{4+} in the oxides, we fit sample spectra between the energies 6520 to 6600 eV in the software package SixPACK (https://www.sams-xrays.com/sixpack), using previously published standards in Johnson et al. (2016).

Synchrotron diffraction data were collected at the undulator beamline 16-IDB (APS, Argonne National Laboratory) using a primary beam energy of 25 MeV (0.4594 Å) and about 94% horizontal polarization, monochromatized by a double-crystal Si (111) monochromator and focused by elliptical mirrors to 2 × 4 μm^2. A basalt clast in the thin section, NWA 7533 C2, was examined. A Pilatus 3× CdTe hybrid-pixel array detector was used for collecting the sample diffraction data. The X-ray beam was initially focused to a rectangular 4 × 5 μm^2 area on the top surface of the thin section, by vertical and horizontal Kirkpatrick-Baez mirrors of 200 mm focal length. Since the beam passed through both the meteorite and the underlying glass slide upon which the sample was mounted, diffraction pattern images were first corrected for diffuse scattering from the glass slide using Dioptas background image subtraction (Hammersley et al., 1996), and then integrated and corrected for geometric distortion from detector tilt using Dioptas (Hammersley et al., 1996). The Mn-rich region in NWA 7533 C2 was scanned in 5 μm steps horizontally and vertically through the focused X-ray beam, and diffraction patterns were recorded in transmission geometry at each step. Rietveld refinement of Mn-oxide structures was conducted with the program PowderCell (Kraus and Nolze, 1996). Preferred orientation along (100) was refined for maghemite, whereas average powder diffraction statistics were assumed for cryptomelane. The structure of the cryptomelane-like manganate was obtained through forward modeling of candidate manganate structures, subsequent LeBail extraction of apparent |F(hkl)| by using a cryptomelane-like low-symmetric supercell with |F(hkl)|'s that were mostly only Friedel-degenerate, thus reducing symmetry-biases as much as possible for powder diffraction data. Structure modeling was conducted with the reversed Monte Carlo approach by using the Endeavour algorithm (Putz et al., 1999). After convergence of the structure model in space group P1, an automatic search for space group symmetries was conducted with the Endeavour software package (Putz et al., 1999). The optimization converged to $R_F = 0.17$. Then local optimization (Putz et al., 1999) was conducted with the assignment of average relative electron densities of Wyckoff sites, using the same approach as in Ma et al. (2019). The chemical composition was obtained by distributing chemical species according to the bulk maganate analysis while keeping the refined relative electron density at each Wyckoff-site fixed.

The converged structure was checked again for possible higher space group symmetries. The final result was used for Rietveld refinement of maghemite and cryptomelane-like manganate with profile terms (U,V, W), the Lorentzian mixing term (na), relative phase proportion, and background as refined parameters. Refinement converged to $wR_p = 0.078$. Pseudo-Voigt profile terms of U,V,W, were 0.98, 0.15, and 0.037, respectively. A mixing term of 0.58 was refined and kept for all phases equally. Finally, the structure of the cryptomelane-like manganate was re-examined by conducting another Le Bail extraction. The extracted |F(hkl)| agree with the structure model to within 7% (the converged R_F was 0.073). The Le Bail refinement converged to a R_p of 0.056 and the fully F(hkl)-weighted wR_p of cryptomelane-like manganate was 0.071. We used the Scherrer equation to estimate the average grain size of the two phases. We obtain 20 ± 5 nm for the cryptomelane-like manganate and maghemite.

The hydrogen contents and D/H values of Mn-oxides in a monzonite clast in NWA 7034 1B, 4 (Fig. S1a) and in a pyroxene clump in NWA 7034 1B, 3 (Fig. S2a), and those of FeOOH in the same sections (Figs. S1h and S2a) were measured in two analytical sessions using a Cameca nanoSIMS 50 L ion microprobe. For both sessions, the sample mount (in epoxy) was degassed in vacuum (~1×10^{-9} Torr) for more than 3 days before the analysis. The vacuum of the analytical chamber was lower than ~1×10^{-9} Torr during data collection. Preliminary D/H values and H abundances from the first session were reported in Liu et al. (2017), where positive secondary ions of H, D, ^{24}Mg, and ^{23}Na were measured with an O^- primary beam of 8 kV and ~0.5 nA. However, later examination indicated that extremely negative δD values in Liu et al. (2017) were an analytical artifact caused by changing peak offsets in H and D after switching sample holders for NWA 7034 and standards. In the second NanoSIMS session, we used a Cs^+ beam of 8 kV and ~ 300 pA to measure negative (−8 kV) secondary ions of H^-, D^-, and $^{18}O^-$, and an e-gun was used for sample charging compensation. Ion images were collected from regions of 25 μm × 25 μm of the pre-sputtered areas. D/H ratios and H abundances were determined from smaller rastered areas (5 μm × 5 μm), with data collected only from the central 80% of these regions. $^{18}O^-$ was used as the reference mass. We do not have a suite of Mn-oxide standards for calibrating the H contents and D/H values, so the SIMS analysis provides only relative variations.

3. Results

3.1. Petrological associations and compositions of Mn-rich regions

All our sections of NWA 7034 and 7533 contain similar mineral and rock clasts (Figs. S1–S8) as previously described for NWA 7034 and pairs in the literature (Agee et al., 2013; Humayun et al., 2013; Santos et al., 2015; Wittmann et al., 2015; McCubbin et al., 2016; Hewins et al., 2017). Interested readers are referred to detailed descriptions and chemical data in Santos et al. (2015), Wittmann et al. (2015), and Hewins et al. (2017). Some lithological clasts in these samples were named inconsistently in previous studies. Both basalts and microbasalts were used to refer to basaltic clasts (Santos et al., 2015; Hewins et al., 2017). We adopt basalts in this study. Breccia clasts were referred to as protobreccias by Santos et al. (2015) and McCubbin et al. (2016), but as clast-laden melt rocks by Humayun et al. (2013) and Hewins et al. (2017). On the basis that the fine-grain matrix in these breccia clasts lack the macroscopic textures consistent with a quenched melt (McCubbin et al., 2016), we also refer to these breccia clasts as protobreccias since they formed before their subsequent entrapment into NWA 7034 and 7533. Rock fragments containing perthite or antiperthite were referred to as monzonite by Humayun et al. (2013) and Hewins et al. (2017) but were described as feldspathic clasts in Wittmann et al. (2015), trachyandesites in Santos et al. (2015), and benmoreite/trachyandesite in Liu et al. (2016). We use monzonite in the following text based on the fact that perthite or antiperthite is typical for monzonite (Hewins et al., 2017). Additionally, melt rocks, melt spherules, and vitrophyres have all been used to refer to spherical clasts and impact melt fragments in the previous studies. Santos et al. (2015) and Wittmann et al. (2015)

grouped spherical clasts as melt spherules. However, Hewins et al. (2017) pointed out that the oval or spherical domains with internal pyroxene clots and plagioclase aureoles were only observed in protobreccias (clast-laden melt rocks). In the following discussion, we adopt the pyroxene clumps from Hewins et al. (2017) for the oval and spherical objects in protobreccias, and used spherules for large rounded clasts. Terrestrial alteration is present in fractures as Ca-carbonate fillings. Pyrite in these breccias was extensively altered to FeOOH with terrestrial like D/H (Lorand et al., 2015).

We observed Mn-rich regions in four types of lithological contexts in all eight sections of NWA 7034 and 7533, including monzonite clasts, pyroxene clumps, basalts, and altered Fe-Ti oxides (e.g., Figs. 1–7 and S1–S8). The most common textural type is fibrous or massive Mn-rich aggregates ($\leq$ 20 μm in the largest dimension) within monzonite clasts (Figs. 2, 5, S1a, b, g, S3a, S4a, b, S6b, S7a, and S8a, d). One such clast was partially assimilated by the fusion crust in NWA 7034 Js2b and Mn-rich glass was observed in the fusion crust derived from this clast (Figs. 2 and S4a). Mn-rich glass is not present in fusion crust formed from matrix or clasts that do not contain Mn-rich regions. The second common type is Mn-rich regions inside pyroxene clumps that contain feldspar aureoles (Figs. 4 and 6). These pyroxene clumps are located inside protobreccia clasts (e.g., Figs. 1 and S2). Compositions of the pyroxene in the clumps are $En_{69-72}Wo_{2-3}$ with oxide totals of 98.7 to 100.8 wt% (Table S1). The third petrological type is Mn-rich regions within basalts (Figs. 3 and S4c). In pyroxene clumps and basalts, Mn-rich regions are often crosscut by or intergrown with nano-crystalline Mg-rich veins (Figs. 3, 4, and 6). The fourth type of occurrence is Mn-rich regions in direct contact with altered Fe-oxides (magnetite with ilmenite lamellae) included in apatite (Fig. 7a) or with Fe-oxide fragments (Figs. 7c and S7b), and Mn-rich region with altered pyrite associated with a plagioclase fragment (Fig. 7b). The Mn-rich regions with >10 wt% Mn are most common in monzonite clasts (Figs. S1–S8). For other textural types, only one occurrence in each type contains Mn up to 33 to 34 wt% (Figs. 3, 4, and 7c). We did not observe any Mn-rich materials in the matrix of the breccias or that of the protobreccias, nor in fractures associated with terrestrial Ca-carbonates acquired during desert weathering.

The volume percentage of Mn-rich regions in each polished section is small (<<1 vol%). Except for Mn-rich glass in the fusion crust of section NWA 7034 Js2b (Figs. 2 and S4a), Mn-rich regions inside the samples contain nano-crystalline aggregates of Mn-minerals, silicates, FeOOH, and possible phosphates. The texture of the Mn-rich regions differs from layered textures in rock coatings or the manganese dendrites in terrestrial samples (e.g., Krinsley et al., 2009; Xu et al., 2010). No diffraction patterns were observed during EBSD analysis, confirming the nano-crystalline nature of phases in these aggregates. From SEM-EDS analyses after normalizing to the anhydrous element total of 100%, the Mn contents in these Mn-rich regions range from 1 wt% to 34 wt% Mn in all petrological occurrences (Figs. S1–S8). Although 1 wt% Mn is already enriched compared to typical igneous and FTP clasts (0.22–0.83 wt% MnO; Humayun et al., 2013; Santos et al., 2015), impact melt rocks (0.34–0.4 wt% MnO; Humayun et al., 2013; Santos et al., 2015), and the matrix (0.35–0.42 wt% MnO; Humayun et al., 2013; Santos et al., 2015), the regions with <5 wt% Mn could be formed by terrestrial alteration of primary minerals or remobilization of other Mn-rich regions with high Mn contents. Therefore, the Mn-rich regions in the following text refer to those with >5 wt% Mn.

Precise compositions of Mn-rich glass and other glasses in fusion crust and Mn-rich regions and other phases were determined with EPMA and are shown in Table 1 (full results in Table S1). The Mn-rich glass contains 4.8–5.6 wt% Mn, much higher than other glasses in the fusion crust (<1.2 wt% Mn, Table S1). The Mn-rich glass also contains noticeably higher amounts of S (0.30 ± 0.06 wt%, $n = 6$) and P (0.14 ± 0.02 wt%, n = 6) than those in other glasses (0.06 ± 0.05 wt% for S and 0.04 ± 0.03 wt% for P, n = 6). Due to dilution by mixing, other elements in the Mn-rich glass (Fe, Ca, Ba, Na) do not show a clear deviation from other glasses in the fusion crust.

The EPMA compositions of Mn-rich regions in clasts vary significantly as a result of increasing amounts of other minerals (e.g., silicates and FeOOH) in these mixtures, but the ranges of variations overlap among different petrological associations (Fig. 8). The Mn and Fe contents in Mn-rich regions are anti-correlated, showing large gradients on a spatial range of 10–20 μm (Figs. 3–5 and 8). For Mn-rich regions with ≥30 wt% Mn, there are still small amounts of silicates present, as indicated by Si + Al of 1.2–4.2 wt% (Tables 1 and S1). Other major elements in Mn-rich regions with ≥30 wt% Mn are Fe (13–19 wt%), Mg (3.2–3.4 wt%), Ca (2.5–3.5 wt%), and Ba (0.9–1.2 wt%) (Tables 1 and S1). Elemental chemistry suggests that the Mn-minerals in the Mn-rich regions are likely Mn-dominant-oxides (confirmed by XANES and XRD below, Figs. 3, 5, and 9).

3.2. Mn valence and mineralogy of Mn-oxides

The near-edge features of the element K-edge XAS spectra were used to assess the electronic structure and valence state of manganese in the samples—quantified by spectral fitting using known standard materials. The Mn K-edge XAS spectrum of Mn-rich glass (5.4 wt% Mn) in the fusion crust of NWA 7034 Js2b differed from those of Mn^{2+}-silicates (Fig. 9) and Mn^{2+} in silicate glasses (Chalmin et al., 2009; De Ferri et al.,

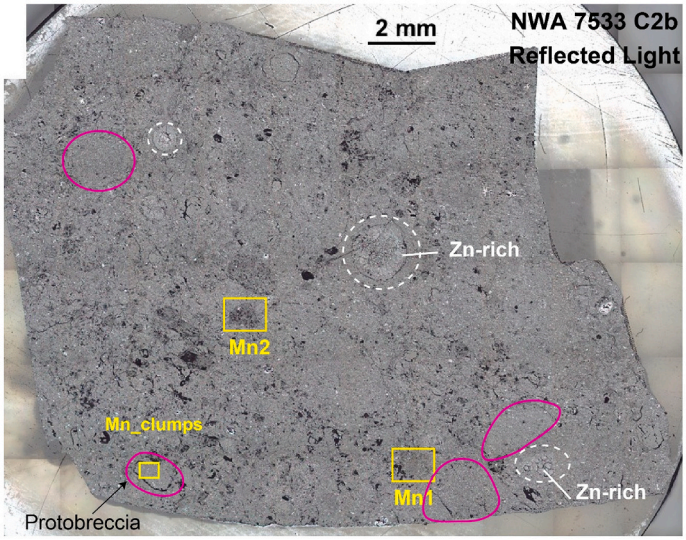

Fig. 1. Reflected light image of NWA 7533 C2b showing the locations of Mn-oxides (boxes) and other features. Mn1 (Fig. 5 and the supplementary file) and Mn2 are Mn-oxides in monzonite clasts. Mn_clumps are pyroxene clumps shown in Fig. 6. Pink lines circle protobreccia clasts and dashed lines circle spherules. Other alteration features in the same section, such as the Zn-rich mineral in spherules (Zn-rich, Liu et al., 2018), pyrite-pyrrhotite assemblages, and detrital apatite grains with Ce-monazites (Liu et al., 2016), are not texturally associated with the Mn-oxides. (For interpretation of the references to color in this figure legend, the reader is referred to the web version of this article.)

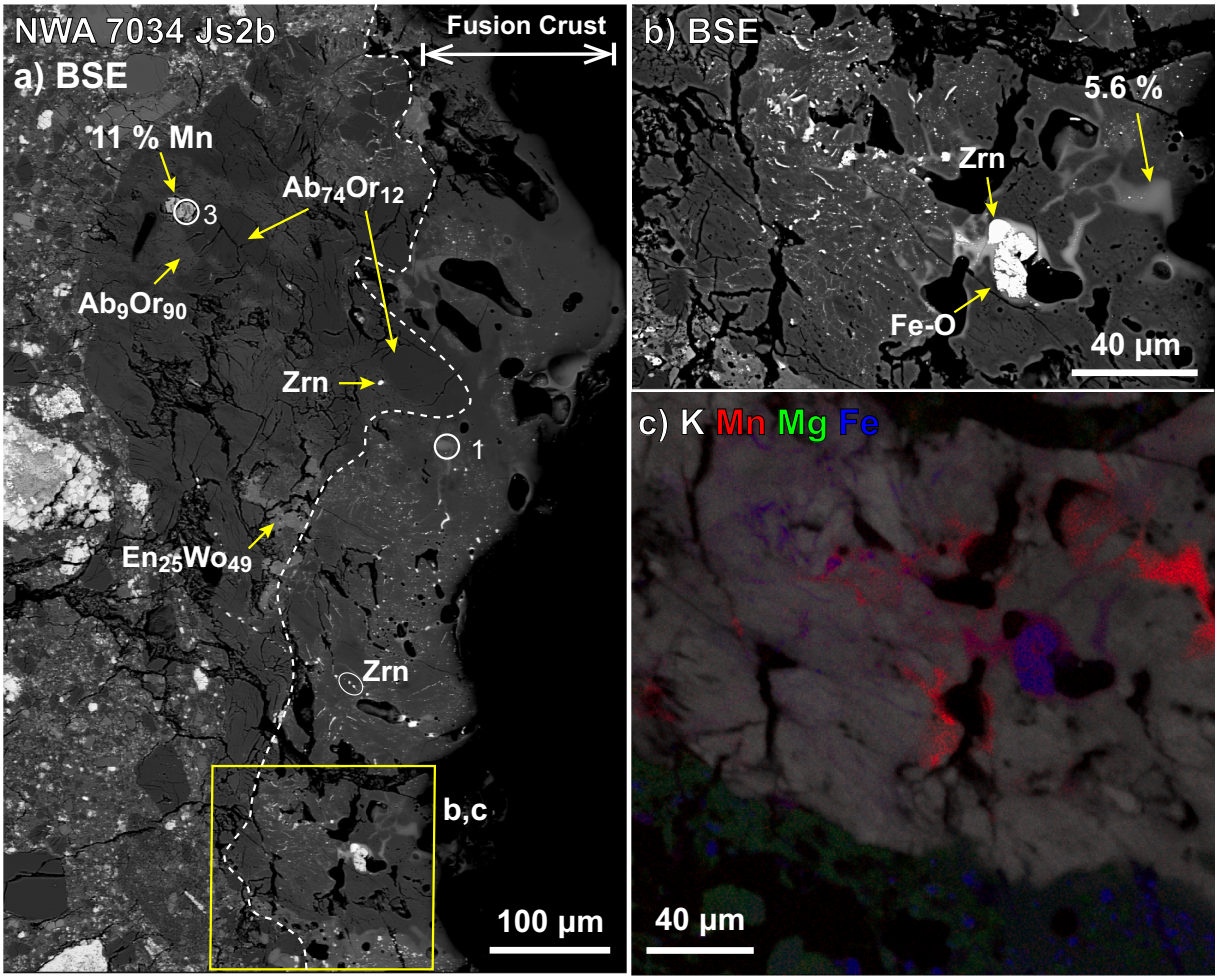

Fig. 2. Evidence for a Martian origin of Mn-oxides in the fusion crust of NWA 7034 Js2b. Mn wt% from EPMA analysis are shown. Circles are the XANES spot analyses with spectra shown in Figs. 8 and S9. a) Backscattered electron (BSE) image showing a Mn-oxides-bearing monzonite clast partially melted into fusion crust. Boxes show locations of subpanel b)-c). The dashed line marks the boundary between the fusion crust and the lithic clast. b) High-magnification view of a region of fusion crust with enriched Mn contents. c) Elemental map of b) showing Mn-rich glass intermixed with those from orthoclase and Fe-oxides. Ab, Albite; Or, Orthoclase; En, Enstatite; Wo, wollastonite; Fe-O, Fe-oxides (likely magnetite); Zrn, zircon. Mineral abbreviations follow Whitney and Evans (2010). The location of this area is shown in Fig. S4 and additional images are shown in Fig. S4a.

2011), revealing inclusions of high-valent Mn species within the glass (Fig. 9).

The Mn K-edge XAS spectra of Mn-rich regions in monzonite clasts showed significant similarity to those of Mn^{4+}-dominant oxides with tunnel or layered structures but differed from those of Mn^{2+}-silicates and anhydrous Mn-oxides (Figs. 5 and 8). Using a known standard Na-birnessite with $Mn^{3.57+}$ (Villalobos et al., 2003) and birnessite SG1 with Mn^{4+} (Webb et al., 2005), the XAS spectra of Mn-rich regions in monzonites were fit by mixing of 24–37% birnessite SG-1 and 74–63% Na-birnessite (e.g., Fig. S9), which translates to 67–73% Mn^{4+} with the rest of Mn being Mn^{3+}. For the XAS spectra of points 1 and 3 in Fig. 5f, fitting produced 85%– 81% Mn^{4+}. Microscale Mn-speciation maps of the monzonite clast (Fig. 5e) and pyroxene clumps with Mn-rich regions (Fig. 6b) in NWA 7533 C2b revealed that Mn-rich regions with >10 wt% Mn are Mn^{4+}-dominant. At small length-scales, significant contamination from neighboring silicates makes the unique identification of Mn speciation difficult for aggregates with <10 wt% Mn (pyroxene clump 2, Fig. 6b).

Synchrotron X-ray diffraction (XRD) patterns of the Mn-rich region in a basalt clast are most consistent with a mixture of ~40–45 vol% of a Ca-rich cryptomelane and 55–60 vol% of a Mg- and Mn-bearing maghemite (Fig. 3). Layered Mn-oxides (e.g., birnessite, vernadite) or Mn-oxides of larger tunnels (e.g., romanechite, todorokite) did not fit the XRD pattern of the Mn-rich aggregates in the mafic clast (the expected strong diffraction peak at low 2θ is missing). The XRD patterns also cannot be fit with goethite (α-FeOOH), lepidocrocite (γ-FeOOH), or akaganeite [Fe(OOHCl)]. The Ca-rich cryptomelane [$(Ca,Na)(Mn^{4+}, Mn^{3+})_8O_{16}$] is a hollandite-type manganate with edge-sharing MnO_6 octahedra forming double chains that link to form tunnels (Post, 1999; Biagioni et al., 2013). Deriving the exact formula is difficult because the composition of the Ca-rich cryptomelane cannot be well constrained given that it is well mixed with the Mn-bearing maghemite. Combined results from XRD and XAS conclusively identified that Mn-rich regions in lithic clasts contain Mn^{4+}-dominant-oxides (hereafter referred to as Mn-oxides) with a hollandite structure.

3.3. *Hydrous nature and hydrogen isotope characteristics of the Mn-oxides*

The low oxide totals (87–98.5 wt%) of the Mn-rich regions in NWA 7034 and 7533 are likely caused by the presence of water and/or pore space within the activation volumes of the electron beams (Tables 1 and S1, Figs. 3 and S2a). The $^{1}H^{+}$, $^{24}Mg^{+}$, and $^{23}Na^{+}$ maps of two Mn-rich aggregates in NWA 7034 1B, 4 show that these elements are heterogeneously distributed within these aggregates, and the H counts in the Mn-rich regions are significantly higher than neighboring silicates (Fig.

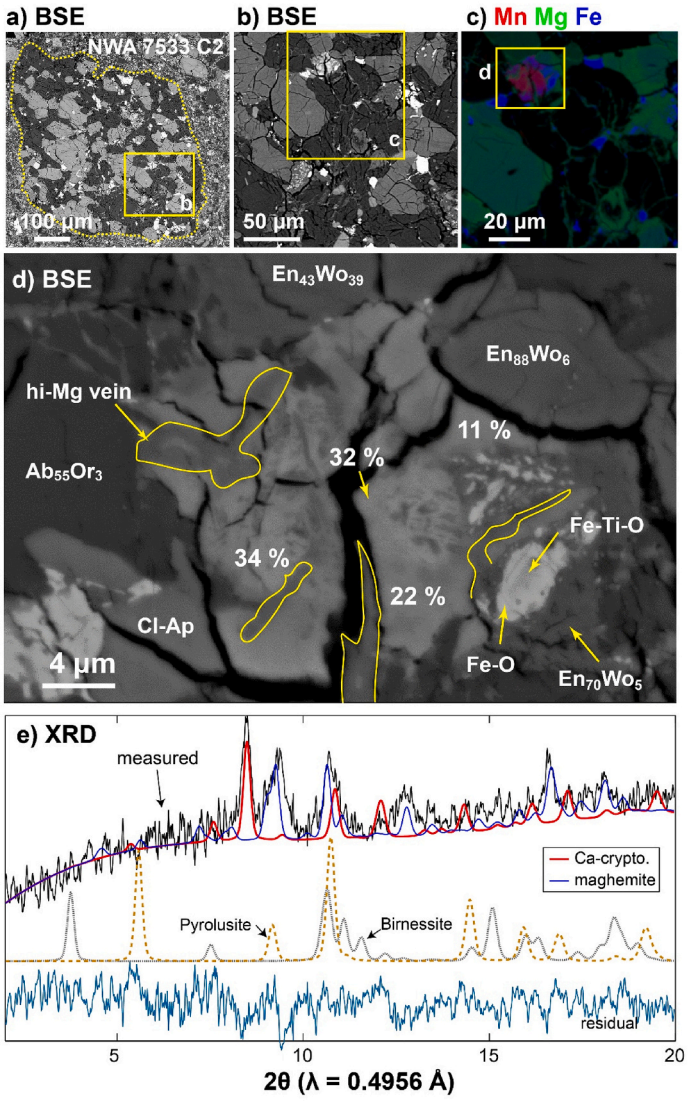

Fig. 3. Mn-oxides in a basalt clast in NWA 7533 C2. a) BSE image of the whole clast outlined by the dotted curve (also Fig. S8b). The box shows the location of the region shown in (b). b) High magnification BSE image showing the context of the Mn-rich region. c) Composite elemental X-ray maps of (b), showing pervasive nano-crystalline high-Mg-silicate veins of an anhydrous composition of $En_{70\pm1}Wo_{4\pm1}$. d) High magnification BSE image of the Mn-rich region. Numbers refer to Mn wt%. Yellow lines mark the high-Mg-silicate veins intergrown with the Mn-oxides. Cl-Ap, chlorapatite; Fe-Ti-O, likely ilmenite. e) An X-ray diffraction (XRD) pattern of the Mn-rich region collected with an X-ray wavelength of 0.4956 Å. The measured curve is best fit by a calculated curve using 40–45 vol% Ca-rich cryptomelane (Ca-crpto.) and 55–60 vol% maghemite. XRD patterns of pyrolusite (MnO_2) and birnessite are from Parise et al. (1998) and (Post and Veblen, 1990), respectively. Additional images of this clast are shown in Fig. S8b. (For interpretation of the references to color in this figure legend, the reader is referred to the web version of this article.)

S1a–b). Moreover, the Mn-rich regions in the spherule in NWA 7034 1B, 3 display higher H counts than FeOOH alteration of pyrite (Fig. S2a). These results indicate that Mn-oxides in the Mn-rich aggregates are hydrous. If one assumes that the instrumental mass fractionation factor for hydrous Mn-oxides and FeOOH are comparable (within 100‰), the D/H values of hydrous Mn-oxides can be estimated from the reported values of FeOOH in the literature ($\delta D = 10 \pm 85$‰ by Lorand et al., 2015). Hydrogen isotope compositions of Mn-oxides in NWA 7034 1B, 3 are -30 ± 42 to $+95 \pm 36$‰, by correcting measurements of FeOOH in the same section analyzed under the exact same analytical conditions to the reported value (Table S2).

3.4. Estimating bulk chemistry of the Mn-oxides-bearing clasts

The bulk chemistry of the Mn-enriched lithic clasts was estimated using average compositions of Mn-rich regions, mineral chemistry from EPMA, and mineral abundances from X-ray maps generated by EPMA or from SEM (Table 3). For the EPMA X-ray maps, modal percentages of major phases were estimated using Mg *K*α, Fe *K*α, and Ca *K*α maps, and converted to weight fraction using densities of these minerals (Table 4). The bulk chemistry of the clast was calculated using the average EPMA compositions of the major phases. From the elemental maps obtained by SEM-EDS, the bulk chemistry of the lithic clasts was directly estimated using the lasso tool in the Oxford AZtec™ software. Both techniques aimed to provide a rough estimate of the bulk chemistry considering the semi-quantitative nature of SEM-EDS method and the inaccuracy in EPMA due to compositional zoning in minerals. In the alkali-silica diagram as in Santos et al. (2015), bulk compositions of Mn-oxide-bearing monzonite clasts (60–63 wt% SiO_2 with 11–12 wt% $Na_2O + K_2O$) reside in the trachyte field and and those of the Mn-oxide-bearing spherule and basalt clast place them in the basaltic field (46–51 wt% SiO_2 and ~ 4 wt % $Na_2O + K_2O$).

4. Discussion

4.1. Evidence for a Martian origin of Mn-oxides

The Mn-rich domains within the glass of the fusion crust imply that NWA 7034 and 7533 carried Mn-rich mineral(s) prior to the arrival of the meteorite on Earth. During the meteorite's rapid traverse through the Earth's atmosphere, intense frictional heating melted a thin layer of the outside of the meteorite that quenched into fusion crust. Owing to the rapid heating and cooling of the object, there was insufficient time to homogenize the melt and thus the composition of the melt mostly represents the protolith minerals (Thaisen and Taylor, 2009). The Mn-rich glass in the fusion crust was only found when the fusion crust cuts across

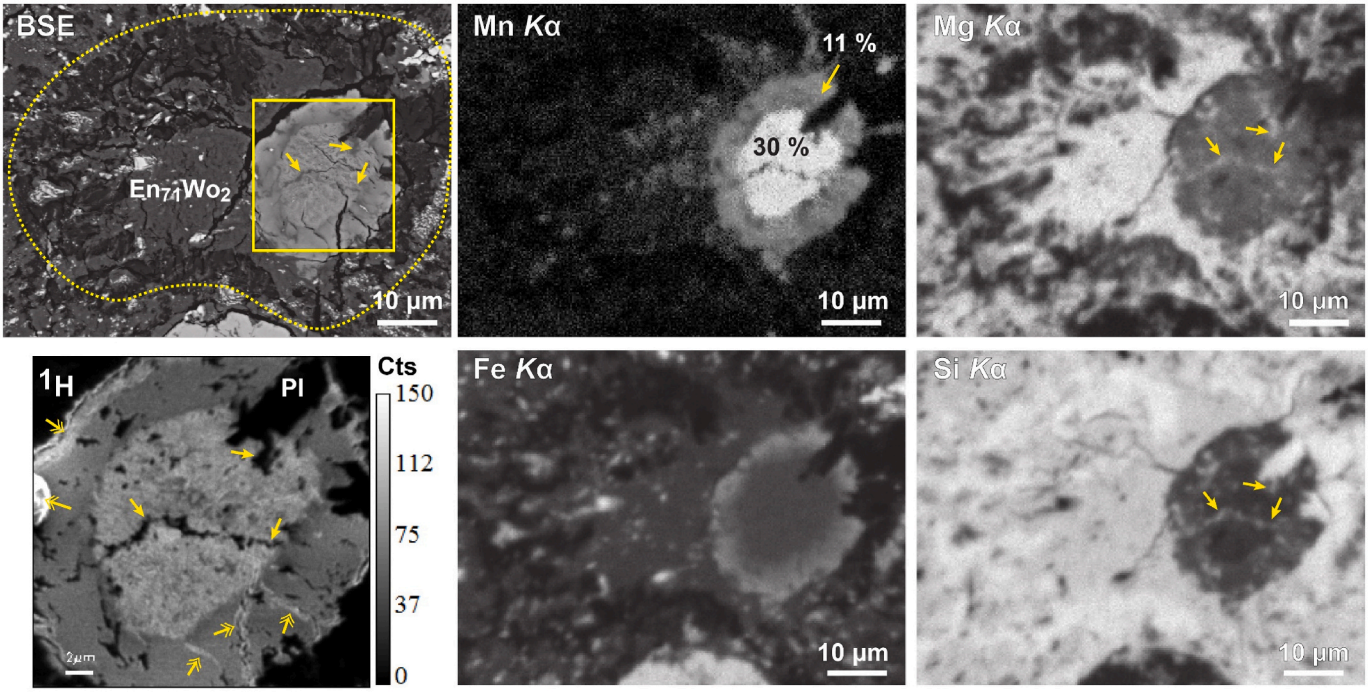

Fig. 4. Mn-oxides in a pyroxene clump in NWA 7034 1B, 3. The outside boundary of the clump is outlined by the dotted curve. The Mn *K*α map shows a strongly zoned region with radiating lobes of slightly higher Mn than the neighboring pyroxene region. Small yellow arrows point to the high-Mg veins that cross-cut Mn-rich aggregates. Double yellow in the ^{1}H map arrows show the H signal from terrestrial contamination in the fractures. EPMA Mn contents in wt% are shown on the Mn *K*α map. Pl: plagioclase ($An_{32}Ab_{64}$). The location of this clump (Mn1) is shown in Fig. S2. (For interpretation of the references to color in this figure legend, the reader is referred to the web version of this article.)

a Mn-oxides-bearing monzonite clast in NWA 7034 Js2b (Fig. 2). Mn-rich glasses were not observed in regions of the fusion crust that are not in contact with Mn-oxides-bearing clasts. As discussed above, the Mn contents (4.8–5.6 wt%) of the Mn-rich glass are much higher than glasses (<1.2 wt%) derived from silicate minerals and Fe-Ti-oxides (Table 1). Moreover, the high-valent Mn domains within the fusion crust is consistent with the notion that the protolith phases included Mn-oxides similar to those observed inside the meteorite—likely admixed with some Mn^{2+} derived from the wholesale melting of the igneous grains associated with the generation of the fusion crust. This relationship implies that Mn-oxides formed in the sample when it was on Mars.

Even with the aforementioned fusion crust observations establishing the Martian origin of Mn-oxides, it is worth evaluating whether terrestrial contamination and alteration formed Mn-rich regions in the main body of the meteorites underneath the fusion crust, especially given signs of terrestrial alteration from D/H values of the Mn-rich region (this study) and FeOOH (Lorand et al., 2015) and from minute clays along grain boundaries in the matrix (Muttik et al., 2014; Leroux et al., 2016). First, the Mn-rich regions in the meteorite main body are not terrestrial. The typical Fe-Mn-oxide coating (desert varnish) from desert weathering (e.g., Dorn, 2013) is absent on the surfaces of NWA 7034 and 7533. Moreover, we did not observe Mn-oxides nor Mn-enrichment in terrestrial Ca-carbonates inside fractures in NWA 7034 and 7533. Rather, these Ca-carbonate-bearing fractures crosscut Mn-oxides in some cases (e.g., Fig. S8), implying that Mn-oxides formed before the Ca-carbonate. Furthermore, the submicron high-Mg silicates (low-Ca pyroxene composition) veins in the Mn-rich regions in pyroxene clumps or the mafic clast (Figs. 3, 4, and 6) suggest Mn-rich regions formed before the high-Mg silicate veins. Because high-Mg silicates are not a typical terrestrial alteration product, both the Mn-oxides and high-Mg silicate veins formed on Mars. Second, the Mn-rich regions with >10 wt% Mn are unlikely formed by terrestrial alteration of primary silicates and magnetite/maghemite in NWA 7034 and 7533, most of which contain <1 wt% Mn (Table S1, Santos et al., 2015; Liu et al., 2016; Hewins et al., 2017). Enrichment of Mn to >10 wt% would require a high degree of alteration, yet these minerals remain mostly pristine. Although primary ilmenite contains higher Mn than silicates, (up to 2.4 wt% Mn, Santos et al., 2015; Liu et al., 2016; Hewins et al., 2017), alteration products of ilmenites contain <5 wt% Mn (Figs. S5b and S7b). Third, we evaluate the possibility that the Mn-rich regions were formed by terrestrial alteration of Martian Mn^{2+}-rich minerals. To date, the only indigenous Mn^{2+}-bearing minerals that have been observed in Martian meteorites are secondary carbonates, including (Ca, Mg, Fe, Mn)CO_3 as zoned concretions or as blocky mixtures in ALH 84001 (Mittlefehldt, 1994), or (Fe, Mn)CO_3 in alteration veins in nakhlites (Bridges and Grady, 2000). Mn contents of these secondary carbonates are typically low (<4 wt% Mn), except for rare siderites with ~15 wt% Mn in Nakhla (Bridges and Grady, 2000). These secondary carbonates in Martian meteorites survived terrestrial alteration, even after 10,000 years in Antarctica (ALH 84001) and ~3000 years (Lafayette) in in terrestrial environment (Jull, 2006). In NWA 7034 and 7533, we did not observe any plausible remnant Martian carbonate within Mn-rich aggregates. Therefore, terrestrial oxidation of a Martian Mn-carbonate precursor is unlikely to explain the observed Mn-oxides. Other potential Mn^{2+} salts ($MnCl_2$, MnS, or MnS_2) have never been reported on Mars or in Martian meteorites. Although Mn-S phases are present in enstatite-rich meteorites, hydrous MnO_2 has not been reported in terrestrial alteration products of (Mn, Fe)S minerals (Bland et al., 2006; Al-Kathiri et al., 2005; Ma et al., 2012; Velbel, 2014). The browneite (MnS) in an enstatite-rich meteorite (Zakłodzie) displays less alteration than nearby troilite (FeS) and the alteration veins dissecting both sulfides only consist of FeOOH (Ma et al., 2012). Additionally, studies of terrestrially weathered chondrites have never reported Mn oxides (Bland et al., 2006; Al-Kathiri et al., 2005). Therefore, the formation of Mn-rich regions by terrestrial alteration is not supported by the combined observations above.

However, the terrestrial-like D/H values of the Mn-rich regions suggest terrestrial overprints. Petrographic evidence shows that Mn-regions formed before the protobreccias (see Section 4.3) and thus

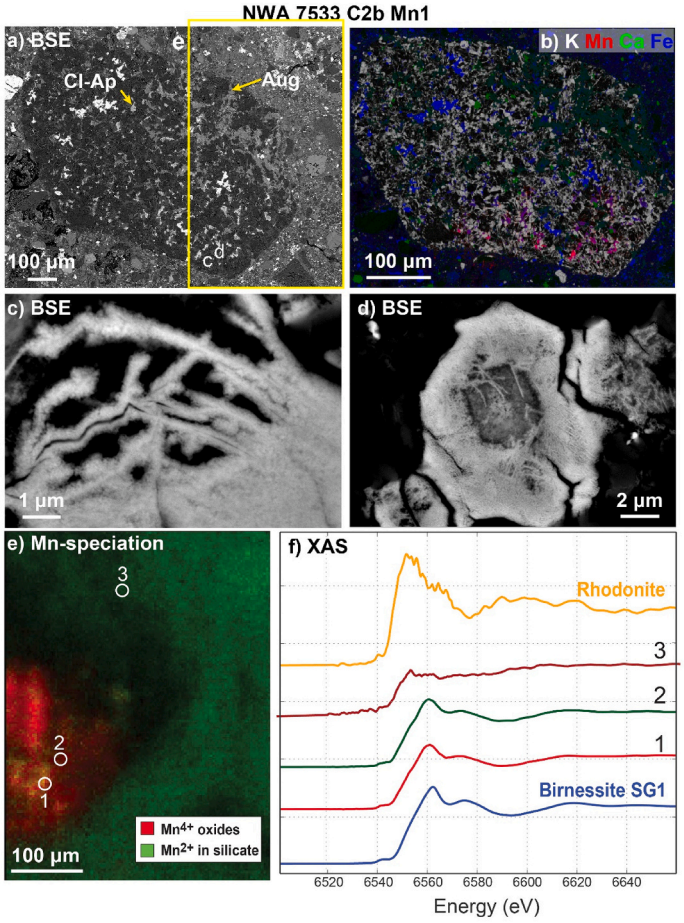

Fig. 5. Mn-oxides in a monzonite clast in NWA 7533 C2b. (a) BSE image of the clast and surrounding fine-grained matrix. Locations of subpanel c)–e) are marked on the BSE image. Image e) extends outside the area a). Aug, augite. (b) Composite elemental map of the clast, showing decreasing Mn content from the edge of the clast toward the interior. Note that the gray color indicates high K content. (c, d) High magnification BSE images of individual Mn-rich regions, consisting of fibrous and massive forms. EBSD analysis yielded no crystal patterns. (e) Redox map of Mn speciation in the area labeled in a), showing predominantly Mn^{4+} in Mn-oxides. Numbers 1 to 3 mark the locations of XAS spectra in f). (f) X-ray absorption spectra (XAS) of Mn-oxides (location 1 and 2 in e) and Mn^{2+} silicate region (location 3 in e). Reference material Birnessite SG1 (Mn^{4+}) was from Webb et al. (2005) and Johnson et al. (2016), and Rhodonite (Mn^{2+}, $MnSiO_3$) from Caltech mineral collection, Butte County, CA. Additional images are shown in Fig. S6a.

Mn-rich regions have likely experienced multiple impact thermal events. These thermal events would have removed the loosely bound H_2O in Mn-oxides. However, previous studies show that minerals in different parts of NWA 7034 and pairs only experienced mild shock pressures of 5–15 GPa (Agee et al., 2013; Wittmann et al., 2015; Leroux et al., 2016). Additionally, Wittmann et al. (2015) suggested that these shock events only generated mild post-shock heating "that were not sufficient to sterilize the water-rich breccias". The final thermal event that lithified different components to form NWA 7034 and pairs was also short because the matrix grains of the breccias show no signs of coarsening (McCubbin et al., 2016). Moreover, Ca-cryptomelane contains a small tunnel structure, which differs from those Mn-oxides of large tunnels or layered structures that are typically in soils and sediments from terrestrial surface weathering (Post, 1999). It may be possible that surface weathering of sediments on Mars produced Mn-oxides of large tunnels or layered structures. As on Earth, these alteration products will contain Ca, Na, Ba, and P derived from the alteration of silicates in the sediments. Subsequently, the repeated mild post-impact heating converted large tunnel or layered Mn-oxides into Ca-cryptomelane but maintained the microcrystalline nature. Owing to the large specific surface area for fine grains, terrestrial water can be easily adsorbed on the surface of these grains. In summary, the Mn-oxides in NWA 7034 and 7533 were most likely generated on Mars, dehydrated during subsequent thermal events, and then rehydrated on Earth.

4.2. Estimating the chemistry of the endmember Mn-oxides

Compared to the composition of Mn-poor glasses from the same clast in the fusion crust, the Mn-rich glass contains noticeably higher amounts of S (0.30 ± 0.06 wt% versus 0.06 ± 0.05 wt%, $n = 6$) and P (0.14 ± 0.02 wt% versus 0.04 ± 0.03 wt%, n = 6, Table 1). This comparison suggests the Martian Mn-mineral likely contains S and P as minor components. However, the non-stoichiometric melting and the dilution of the Mn-oxides into the fusion crust make it difficult to extract the end-member composition of Mn-oxides.

To estimate the end-member chemistry of Mn-oxides, we examine elemental correlations in various Mn-rich regions from different lithological types (Figs. 8 and S10). To avoid significant interference from other minerals, we use only the EPMA data of Mn-rich regions with >0.09 mol/g of Mn (>5 wt%) and <9 wt% Si. As shown in the molar Mn/Fe versus molar (Si + Al) plot (Fig. 8a), data of Mn-rich regions are bounded by FeOOH (goethite) or Fe oxides, low-Ca pyroxene, and the Mn-mineral with a high Mn/Fe ratio at Si + Al = 0. Using additional element/Fe ratios versus molar (Si + Al) plots, the element/Fe ratios in the contamination-free Mn-mineral can be estimated based on the mixing of these three components (Table 2, Figs. 8 and S10). The Fe content (~14 wt%) in the Mn-mineral was estimated by bounding the data using these three components in the Fe wt% versus molar (Si + Al) plot (Fig. 8b). With the derived Fe content (14 wt%) and lower bounds of molar elemental ratios for the Mn-mineral, we inferred compositions of the Mn-oxides (Table 2). Data of the Mn-rich glass in fusion crust were not used in the above calculation. The presence of Fe, P, and S in the inferred Mn-oxide compositions provide additional support that the Mn-oxides are sources of the Mn-rich glass in the fusion crust.

4.3. Timing of Mn-oxides formation in NWA 7034 and pairs

As a regolith breccia containing polymict fragments, NWA 7034 and pairs have a complex assembly history. Combining the sequence of formation by Hewins et al. (2017) with other information reported in the

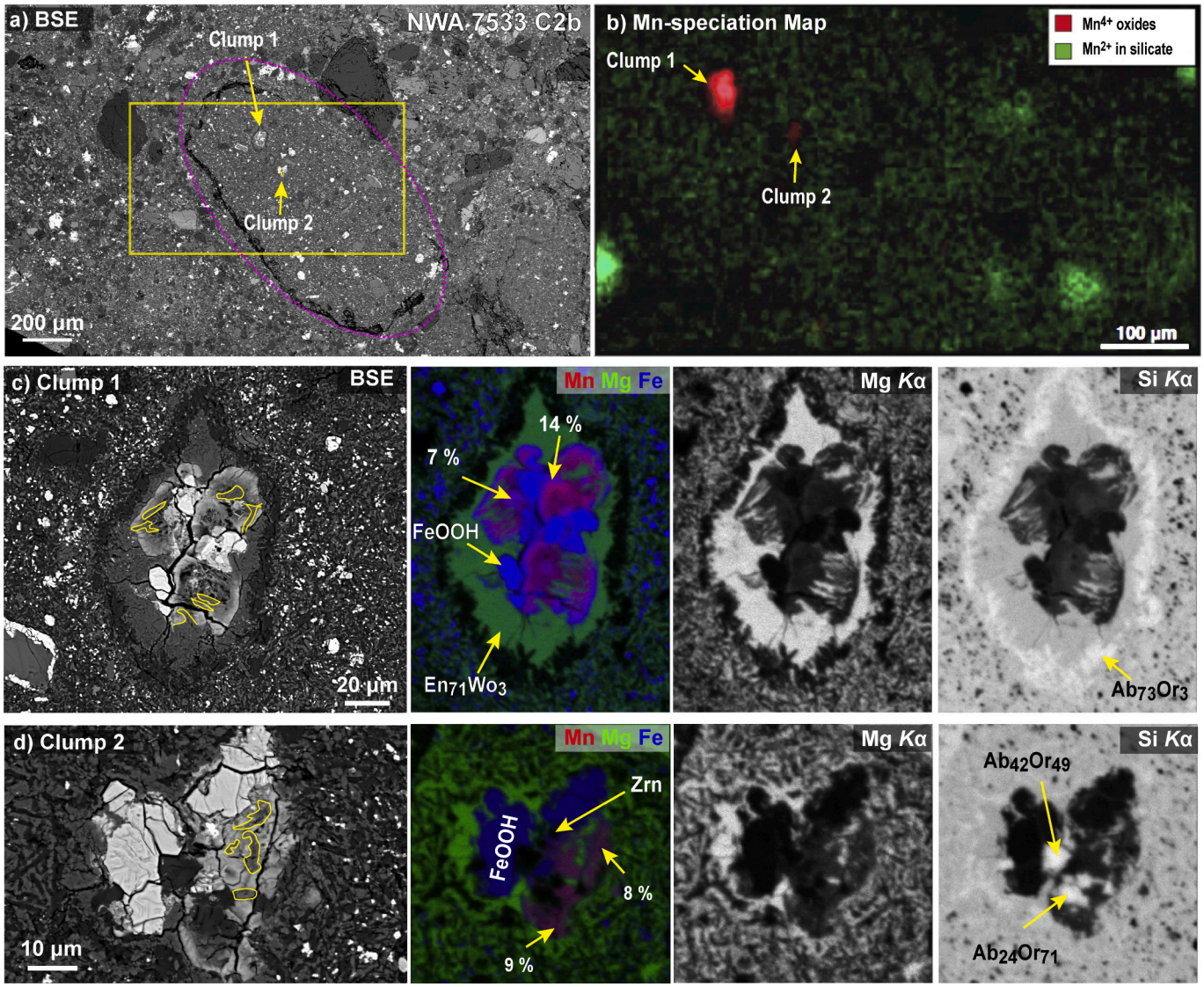

Fig. 6. Mn-oxides in pyroxene clumps in NWA 7533 C2b. a) BSE map showing locations of the clumps in a protobreccia clast (purple ellipse). The yellow box marks the location of the XAS Mn speciation map in (b). Clump 2 with <10 wt% Mn is not clearly discernable in b), suggesting that most Mn is 3+. c) BSE and X-ray intensity maps of Clump 1. d) BSE and X-ray intensity maps of Clump 2. Yellow lines in the BSE images demarcate the Mg-silicate veins. High magnification BSE images of Mn-oxide regions are shown in Fig. S7c–d. (For interpretation of the references to color in this figure legend, the reader is referred to the web version of this article.)

literature, we propose a modified sequence of formation in the following stages. In Stage 1, monzonite with ancient zircons crystallized in the Martian crust at >4.4 Ga (Humayun et al., 2013; McCubbin et al., 2016; Hewins et al., 2017). Norite was linked to crustal province of similar ages based on the association of orthopyroxene and plagioclase with monzonite and ages of pyroxenes (Nyquist et al., 2016; Hewins et al., 2017). Additionally, alkali basalts likely erupted and crystallized in the same period based on U-Pb ages of a zircon grain in an alkali basalt fragment (McCubbin et al., 2016). Subsequent impacts excavated the crustal norite and monzonite and mixed with the Martian surface rocks (alkali basalts) and regolith. At a later time (Stage 2), pyroxene clumps with feldspar aureoles formed in impact plumes and deposited on the surface. In Stage 3, protobreccias formed by additional impacts of a surface area containing the pyroxene clumps and above rock fragments, because mineral fragments in protobreccias are similar to those in rock fragments in NWA 7034 and pairs (McCubbin et al., 2016). It is worth noting that the macroscopic texture of the matrix in the protobreccia is inconsistent with impact melting during its formation (McCubbin et al., 2016). In Stage 4, alteration veins (feldspar or Fe-oxides) formed in different impact-produced fragments, because these veins are truncated at the boundaries between their host clasts (a spherule and a protobreccia) and the matrix of NWA 7034 and 7533 (McCubbin et al., 2016; Hewins et al., 2017). In Stage 5, an impact event lithified all these components to become NWA 7034 and pairs, but the impact did not cause melting of the matrix (McCubbin et al., 2016). The age of Stage 5–the final lithification that formed NWA 7034 and 7533–was suggested to be 1.35 Ga (Hewins et al., 2017) or 1.5 Ga (McCubbin et al., 2016). Finally, before excavation, pyrite veins and disseminated euhedral pyrite grains formed during or after NWA 7034 and 7533 lithified since they were observed in diverse petrological types in NWA 7533 (Lorand et al., 2015). Timing of basalt or andesitic basalt fragments in the assembly of NWA 7034 and pairs is unclear since U-Pb ages of apatite in these rock fragments appear to be reset by the thermal event at Stage 5. Additionally, Leroux et al. (2016) suggested magnetite and silica inclusions in pyroxenes were produced by a metamorphic event that decomposed pyroxene. The timing of this event is also unclear.

Based on the petrological occurrences of Mn-oxides, we can infer the relative timing of Mn-oxides in the assembly of NWA 7034 and pairs.

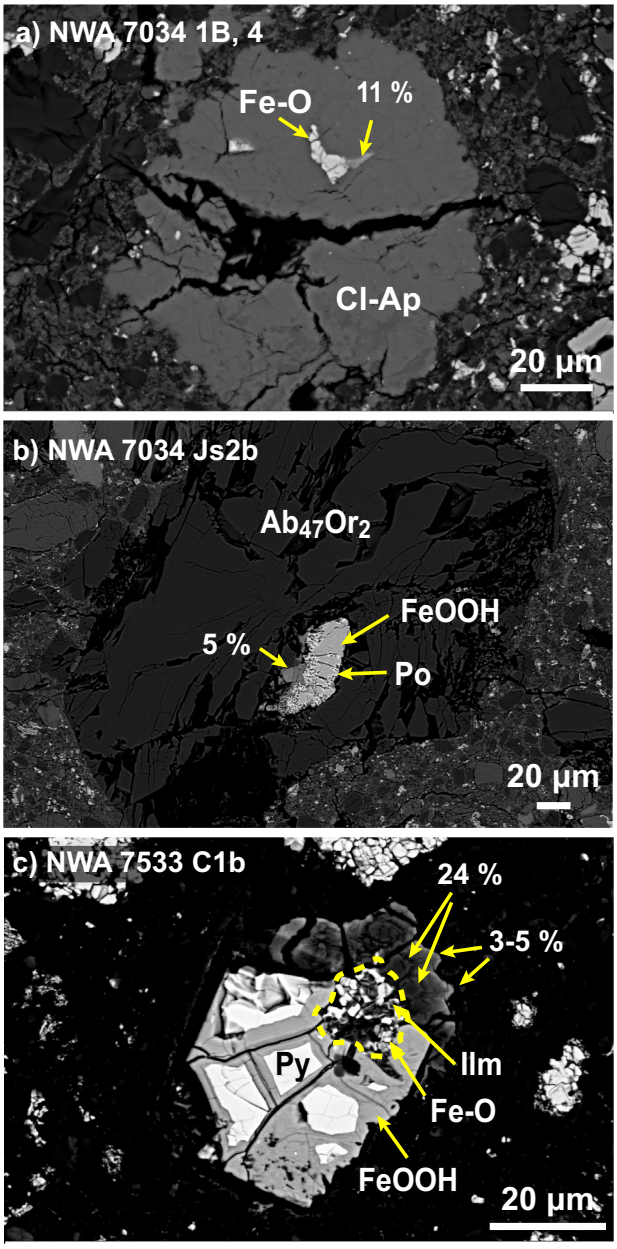

Fig. 7. Additional petrological associations of Mn-rich regions. (a) Occurrence with Fe-oxides (Fe-O) in a chlorapatite (Cl-Ap) in NWA 7034 1B, 4. (b) Occurrence with pyrrhotite (Po) and FeOOH (alteration of pyrite) inside a plagioclase grain in NWA 7034 Js2b. (c) Occurrence with altered Fe-oxides in contact with an altered pyrite (Py) in NWA 7533 C1b. Ilm, ilmenite. Additional images of these occurrences are shown in Figs. S1g, S4b, and S5a, respectively.

The lack of Mn-rich regions in the matrix of NWA 7034 and 7533 suggests Mn-oxides were not produced after the lithification of NWA 7034 and 7533 on Mars. The occurrences of Mn-rich materials in both intrusive (monzonite), extrusive (basalt), and surface (clumps) rocks further indicate that fluid alteration did not occur in the source protoliths of these rock fragments, especially considering the different delivery times of different lithology types to the surface area that formed NWA 7034 and pairs (Hewins et al., 2017). More importantly, our observation of Mn-oxides in pyroxene clumps but not in the matrix of protobreccias indicates that Mn-oxides did not form after the formation pyroxene clumps. Therefore, Mn-oxides likely formed before the final lithification of NWA 7034 and 7533 (>1.35 Ga) but subsequent to the formation of pyroxene clumps. Unfortunately, the absolute ages of Stage 2 and 3 are currently unknown. Thus, an upper age limit of Mn-oxides is loosely placed to be no older than the crystallization age of crustal rocks (4.4 Ga).

4.4. Formation of Mn-oxides on Mars

Manganese is a minor element in basaltic Martian crust at a concentration (< 0.4 wt% MnO) that is a factor of >60 lower than Fe (~18 wt% FeO) (Taylor and McLennan, 2008; Taylor, 2013). However, the Mn-rich regions in NWA 7034 and 7533 contain up to 42 wt% MnO whereas Mn-rich materials in sedimentary rocks at Endeavour and Gale craters contain MnO up to 17 wt% (Arvidson et al., 2016; Lanza et al., 2016; Meslin, 2018; Gasda et al., 2019). Therefore, to form Mn-rich rocks, Mn is released by chemical weathering of crustal rocks and subsequently fractionated from more abundant Fe.

Morphological and mineralogical observations of the Martian surface showed that chemical weathering was prevalent in the Noachian and the early Hesperian period (e.g., Ehlmann et al., 2011 and references therein), providing the mechanism to release Mn from the crustal rocks. Enrichment of Mn in sedimentary record can be achieved after significant evaporation of a long-lasting water body during which other more abundant cations are removed by early precipitation (Berger et al., 2019). Alternatively, oxidation of dissolved Mn^{2+} in aqueous solutions can deposit Mn-oxides. Both mechanisms require sustained water activities, because Mn^{2+}(aq) has a longer residence time than Fe^{2+}(aq) owing to the slow oxidation kinetics of Mn^{2+}(aq) than Fe^{2+}(aq) (Morgan, 2005). The frequent occurrences of Mn-oxides in the 240+ m exposure of sedimentary rocks at Gale crater (Gasda et al., 2019) are consistent with the idea that large bodies of water existed and were stable for 100 to 10,000 years and may have formed and disappeared repeatedly from ~3.6 to 3.2 Ga (Grotzinger, 2015).

Thermodynamically, reactions of Mn^{2+}(aq) to MnO_2 or Mn_2O_3 in surface fluids (pH = 7) occur in oxidizing environments (Eh > +0.5 V). Several alternative mechanisms were proposed. First, a recent experimental study showed that MnO_2 can be produced under anoxic conditions by a disproportional transformation of hausmannite (Mn_3O_4) reacting with highly acidic (pH < 3) solutions (Luo et al., 2018). The hausmannite precursor could have formed in alkaline solutions (pH > 6) in less oxic solutions (Eh < +0.5 V, Noda et al., 2019, Fig. S11). If this is the mechanism, the very acidic solution (pH < 3) that formed MnO_2 would produce secondary silica and Fe-bearing sulfate (jarosite) (Noda et al., 2019). Neither of these secondary phases was observed with Mn-oxides in NWA 7034 and 7533. Moreover, P contents in Mn-rich regions in NWA 7034 and 7533 indicate the possible presence of microcrystalline phosphate, which implies the fluids that deposited the Mn-oxides are not acidic (Hurowitz and McLennan, 2007). These observations in NWA 7034 and 7533 are similar to the lack of relevant secondary minerals or significant alteration of substrate minerals in Mn-rich materials at Gale crater (Noda et al., 2019). Second, redox potential of a aqueous system is controlled by the redox couples present. Experiments reacting Fe-bearing minerals with pure water in 1-atm CO_2 demonstrated that solutions were oxic owing to the buffering effect by the Fe^{3+}/Fe^{2+} redox couple (Baron et al., 2019). However, Mn in typical rock-forming minerals is dominantly Mn^{2+} and thus the aqueous system in O_2-depleted atmosphere will be buffered mainly by the Fe^{3+}/Fe^{2+} redox couple if no other strong oxidants are available (e.g., oxychlorine compounds). Such a system still lies in the stability field of Mn^{2+}(aq) not those of Mn-oxides (Noda et al., 2019, Fig. S11). Third, direct UV oxidation of Mn^{2+} and microbial oxidation are also means to achieve the required high redox potentials in solutions (Anbar and Holland, 1992; Morgan, 2005). Given the absence of direct evidence for microbial life on Mars, there is no current need to lean on explanations involving microbial oxidation—even though it is the main mode of manganese oxidation on Earth today (Tebo et al., 2004). Last, UV oxidation is inefficient when there is a significant amount of Fe in the fluid (Anbar and Holland, 1992). The high Fe contents (>16 wt% Fe) associated with

Table 1
Selected EPMA data of Mn-rich regions and other phases in different lithologies[1]

	d.l.[2]	7533 C2b Mn1 Monzonite (Fig. 5)		7034 1B3 Px Clump (Fig. 4)		d.l.[2]	7034 Js2b Fusion Crust (Fig. 2)			7533 C2 Mn2 Basalt (Fig. 3)				
wt%	wt%	Mn-rich	FeOOH	Core	Rim	wt%	Mn-rich Gl[3]	Silicate Gl[3]	Fe-rich Gl[4]	Mn-rich	Hi-Mg vein	Fe-O	low-Ca vein[5]	low-Ca px
Elements														
Si	0.02	1.17	2.28	5.06	7.12	0.01	23.6 ± 0.4	27.9 ± 2.8	21.6	1.58	16.9	2.03	24.4	24.3
Ti	0.03	0.03	0.04	0.03	0.03	0.02	0.16 ± 0.07	0.28 ± 0.06	1.41	0.03	0.19	4.97	0.17	0.21
Al	0.02	0.43	0.03	1.15	1.28	0.01	7.39 ± 1.43	6.56 ± 4.52	1.19	0.61	1.57	0.67	1.00	0.16
Fe	0.05	18.2	57.8	14.4	32.9	0.03	8.33 ± 0.42	3.64 ± 4.30	22.0	13.4	13.4	58.7	12.9	16.8
Mg	0.03	3.26	0.38	7.22	6.43	0.01	2.21 ± 1.16	5.06 ± 3.79	2.04	3.15	10.3	1.78	14.5	12.4
Ca	0.01	2.68	0.73	1.06	1.09	0.01	3.57 ± 1.69	6.54 ± 6.42	11.1	3.33	1.64	0.24	1.44	2.12
Na	0.05	0.21	0.15	0.28	0.33	0.02	1.61 ± 0.46	1.54 ± 0.97	0.27	0.22	0.11	0.02	0.04	0.06
K	0.01	0.14	0.03	0.18	0.22	0.01	3.30 ± 1.31	3.87 ± 3.74	0.66	0.12	0.07	0.01	0.01	0.01
Cr	n.d.	n.d.	n.d.	n.d.	n.d.	0.03	b.d.	b.d.	b.d.	b.d.	0.06	0.41	b.d.	0.05
Mn	0.04	31.6	0.37	29.6	10.0	0.03	5.22 ± 0.26	0.39 ± 0.41	0.60	33.6	9.78	0.89	0.60	0.84
Ni	0.06	0.15	0.06	0.09	0.21	0.04	b.d.	b.d.	b.d.	0.34	0.15	0.26	b.d.	b.d.
Zn	0.10	b.d.	b.d.	b.d.	b.d.	0.07	b.d.	b.d.	b.d.	b.d.	b.d.	b.d.	b.d.	b.d.
Cl	n.d.	n.d.	n.d.	n.d.	n.d.	0.01	0.05 ± 0.01	0.02 ± 0.02	0.11	0.36	0.20	0.01	0.12	0.03
S	0.01	0.42	0.28	0.48	0.25	0.01	0.30 ± 0.06	0.04 ± 0.05	0.65	0.35	0.14	b.d.	0.02	b.d.
P	0.04	0.97	0.06	0.29	0.54	0.03	0.14 ± 0.02	0.02 ± 0.03	0.18	0.78	0.27	b.d.	0.26	b.d.
Ba	0.08	1.13	b.d.	0.26	0.12	0.06	b.d.	b.d.	0.07	1.08	0.39	0.07	b.d.	b.d.
O	0.15	36.4	35.7	36.2	36.7	N/A	42.3[6]	44.0[6]	33.0[6]	33.0[6]	40.4[6]	24.9[6]	43.2[6]	42.3[6]
Total		96.8	97.8	96.3	97.2									
Oxides[6]														
SiO_2	0.05	2.50	4.89	10.8	15.2	0.02	50.5 ± 0.8	59.7 ± 6.1	46.3	3.38	36.1	4.34	52.3	52.1
TiO_2	0.05	0.05	0.06	0.05	0.05	0.04	0.27 ± 0.11	0.46 ± 0.11	2.36	0.05	0.32	8.29	0.29	0.35
Al_2O_3	0.04	0.82	0.06	2.18	2.42	0.01	14.0 ± 2.7	12.4 ± 8.5	2.25	1.15	2.97	1.26	1.88	0.30
Fe_2O_3	0.07	26.1	82.6	20.6	47.1	0.04	N/A	N/A	N/A	19.2	19.1	N/A	N/A	N/A
FeO	0.06	N/A	N/A	N/A	N/A	0.04	10.7 ± 0.5	5.21 ± 6.15	28.3	N/A	N/A	75.5	16.6	21.6
MgO	0.04	5.41	0.63	12.0	10.7	0.01	3.67 ± 1.92	5.59 ± 6.51	3.39	5.23	17.1	2.95	24.0	20.6
CaO	0.02	3.75	1.02	1.48	1.52	0.01	4.99 ± 2.37	9.15 ± 8.98	15.5	4.66	2.3	0.34	2.02	2.97
Na_2O	0.07	0.29	0.21	0.37	0.44	0.02	2.16 ± 0.62	2.07 ± 1.31	0.37	0.30	0.15	0.02	0.05	0.09
K_2O	0.01	0.17	0.03	0.22	0.26	0.01	3.97 ± 1.58	4.67 ± 4.51	0.80	0.15	0.09	0.01	0.02	0.01
Cr_2O_3	n.d.	n.d.	n.d.	n.d.	n.d.	0.04	b.d.	b.d.	b.d.	b.d.	0.08	0.61	b.d.	0.07
MnO_2	0.07	49.9	0.59	46.8	15.8	0.04	N/A	N/A	N/A	53.2	15.5	N/A	N/A	N/A
MnO	0.05	N/A	N/A	N/A	N/A	0.04	6.74 ± 0.33	0.62 ± 0.65	0.78	N/A	N/A	1.15	0.78	1.08
NiO	0.07	0.19	0.07	0.12	0.26	0.05	b.d.	b.d.	b.d.	0.44	0.20	0.33	b.d.	b.d.
ZnO	0.12	b.d	b.d.	b.d.	b.d.	0.08	b.d.	b.d.	b.d.	b.d.	b.d.	b.d.	b.d.	b.d.
Cl	n.d.	n.d.	n.d.	n.d.	n.d.	0.01	0.05 ± 0.01	b.d.	0.11	0.36	0.20	0.01	0.12	0.03
SO_3	0.03	1.05	0.69	1.20	0.63	0.03	0.74 ± 0.14	0.21 ± 0.1	1.63	0.88	0.35	0.02	0.05	b.d.
P_2O_5	0.09	2.23	0.13	0.67	1.24	0.06	0.31 ± 0.04	0.14 ± 0.05	0.42	1.78	0.62	b.d.	0.60	b.d.
BaO	0.08	1.27	b.d.	0.29	0.13	0.07	b.d.	b.d.	0.08	1.21	0.44	0.07	b.d.	b.d.
Total		93.8	91.0	96.8	95.8		98.1	100.0	106	92.0	95.5	94.9	98.7	99.3

[1] The full set of EPMA data from three different analytical sessions is reported in Table S1. n.d., not determined; b.d., below detection. N/A: not applicable.
[2] Detection limits were calculated based on counting statistics. The first set of detection limits was for analyses of 7533C2b Mn1 and 7034 1B3 Clump obtained at 15 kV and 5 nA. The second set of detection limits was obtained at 15 kV and 10 nA.
[3] These data represent the average and one standard deviation of 6 points. Gl, glass.
[4] This point analyzed a mixture of glass, Fe-S and Fe-O, which yielded a high total. Although this is regarded to be a bad analysis, we use it to demonstrate that assimilation of Fe-sulfide and Fe-oxide in the fusion crust cannot generate high Mn in the Mn-rich glass.

[5] This point was obtained on low-Ca pyroxene veins inside the basaltic clast. Analyses of low-Ca veins inside the Mn-rich region are invariably affected by the Mn-oxides.

[6] Oxygen concentrations and oxide contents were calculated by assumed valence states of elements. For Mn-oxides and FeOOH, all Mn and Fe are assumed to be 4+ and 3+ respectively, for silicates and Fe-oxides, all Mn and Fe are assumed to be 2+.

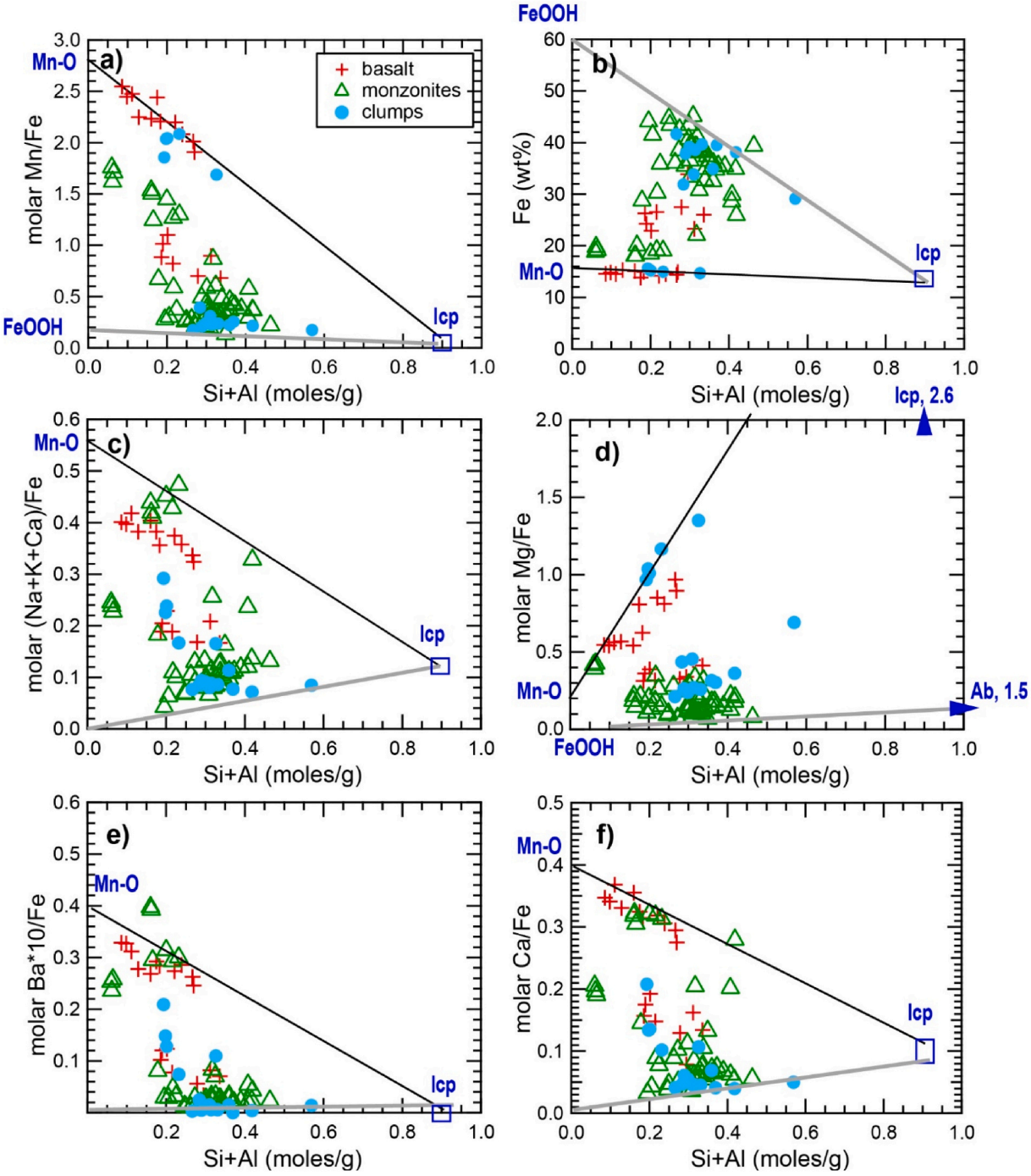

Fig. 8. Estimation of the composition of the end-member Mn-oxides (Mn-O) from EPMA analysis of different Mn-rich regions. Different symbols are used for different petrological associations of Mn-oxides. Only data with >0.05 mol of Mn and < 9 wt% Si are plotted to avoid scattering caused by significant silicate contamination (Table S1). Moles of elements and wt% of Fe are calculated after normalizing EPMA totals to 100%. Lines show the bounds of mixing between three components: Mn-oxides, FeOOH, and low-Ca pyroxene (lcp). Thick gray lines show mixing between FeOOH and low-calcium pyroxene (lcp, $En_{\sim 70}Fs_{\sim 28}Wo_{\sim 2}$) and the black lines show the likely mixing line between Mn-oxides and low-calcium pyroxene. In d), an additional component shows a small effect of feldspar (Ab) with a molar Mg/Fe of ~1.5.

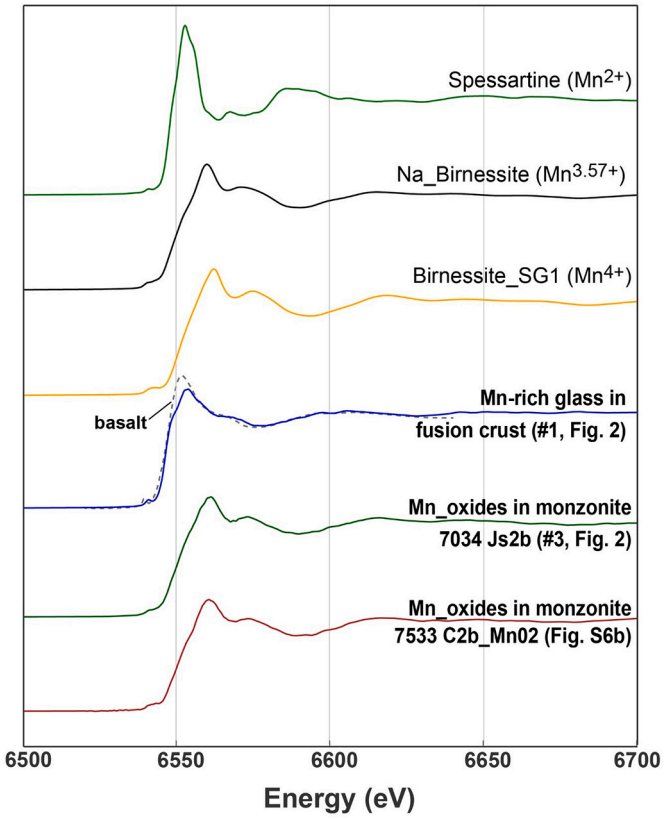

Fig. 9. Mn K-edge X-ray absorption spectra of Mn-rich glass in the fusion crust and Mn-oxides in monzonite clasts, in comparison to reference materials of spessartine ($Mn_2Al_3Si_4O_{12}$), Na_birnessite ($Mn^{3.57+}$), and birnessite_SG1 (Mn^{4+}). The Mn valences of the reference birnessites are directly measured by Villalobos et al. (2003) and Webb et al. (2005). The spessartine standard was used in Johnson et al. (2016). The basalt spectrum is from Chalmin et al. (2009).

the Mn-oxides in NWA 7034 and 7533 and with high-Mn rocks on Mars imply that UV oxidation is not the main process that produced these Mn-oxides. The geological contexts of Mn-rich materials on Mars (e.g., fracture fills; Lanza et al., 2016) also indicate that the environment that Mn-oxides formed did not have direct contact with UV light. Therefore, the formation of Mn-oxides on Mars likely involved high-Eh materials.

High-Eh materials on Mars include dissolved atmospheric O_2 or its products from UV radiation (e.g., hydrogen peroxide or oxychlorine compounds) in aqueous fluids (Lanza et al., 2014; Lanza et al., 2016; Lasne et al., 2016). Perchlorate, one form of oxychlorine compounds, has been directly measured in the polar regolith (Hecht et al., 2009; Kounaves, 2010) and inferred at Gale crater (Glavin, 2013). However, perchlorates are kinetically inhibited from reaction when dissolved in water (Brown and Gu, 2006; Hecht et al., 2009; Mitra and Catalano, 2019). Other, more reactive oxychlorine species (e.g., ClO_3^-, ClO_2^-, ClO^-) could be an alternative (Kounaves et al., 2014; Mitra and Catalano, 2019), but in situ measurements on the Martian surface (Hecht et al., 2009; Hogancamp et al., 2018) or high-precision measurements of Martian meteorites (Kounaves, 2010) have not directly detected these species. Hydrogen peroxide (H_2O_2) has been observed in the modern-day Martian atmosphere at 10s' of ppb level and may be present in early Mars (Lasne et al., 2016), but alteration experiments showed that H_2O_2 in solutions can generate Mn^{3+}-oxides but is incapable of converting Mn^{2+}(aq) into Mn^{4+}-oxides (Noda et al., 2019). Despite of the potential shortfalls as suggested above, these O_2 products may be stored in sediments and provide an O_2 source for aqueous oxidation reactions. Since O_2 products require atmospheric O_2, their involvement in forming oxidized Mn in geological record indicates the presence of O_2 in Martian history. The modern-day Mars atmosphere contains ~1450 ppm O_2 (Mahaffy et al., 2013) and is thought to be produced photochemically with CO_2 and H_2O in the atmosphere (Zahnle et al., 2008). However, the presence and concentration of atmospheric O_2 over the Mars' history are uncertain, although its presence was inferred through oxygen isotopes and modeling (see references in Ward et al., 2019). Together with Mn-rich materials in sedimentary rocks of different ages, the presence of oxidized Mn in regolith before 1.35 Ga as inferred from NWA 7034 and 7533 implies that atmospheric O_2 may have been present before 1.35 Ga.

Although atmospheric O_2 on Mars provides the required redox potential, the formation of Mn^{4+}-oxides from aqueous solutions is also controlled by kinetics, which is a function of Mn^{2+}(aq) concentration, the presence of catalysts, dissolved O_2 abundances, and temperature. Dissolved O_2 abundances in surface solutions depend on the atmospheric O_2 content and pressure. In the modern-day oxygenated Earth

Table 2
Estimated bulk compositions of Mn-bearing clasts and Mn-rich regions.

	Monzonites								Pyroxene clump		Basalt			
	7533 C2 Mn4 (SEM-EDS)				7533 C2 Mn1 (SEM-EDS)		7034 Js1b Mn1 (Fig. S3a)[a] (EPMA)	7533 C2b (Fig. 5)[a] (EPMA)	7034 1B, 3 (Fig. 4) (EPMA)		7533 C2 Mn2 (Fig. 3) (SEM-EDS)			
	Bulk		Mn-rich region		Bulk		Bulk	Bulk	Bulk[a]	Mn-rich region (n = 13)	Bulk		Mn-rich region	
Oxide	wt%	1σ[b]	wt%	1σ	wt%	1σ	wt%	wt%	wt%	wt%	wt%	1σ	wt%	1σ
SiO_2	60.5	0.12	27.4		61.5	0.08	60.5	62.3	46.0	19.8	50.9	0.11	26.3	0.05
TiO_2	0.19	0.04			0.20	0.03	0.05	0.08	0.18	0.28	0.55	0.04	0.54	0.03
Al_2O_3	16.9	0.07	8.16	0.16	18.0	0.05	19.4	16.2	11.0	2.55	14.2	0.06	4.56	0.03
FeO	2.50	0.07	43.4	0.33	5.10	0.05	3.77	4.21	13.98	31.3	11.8	0.08	27.9	0.07
Cr_2O_3											0.16	0.04		
MnO	0.16	0.05	5.37	0.19	0.40	0.03	1.28	0.32	6.61	26.7	0.32	0.04	19.9	0.06
MgO	2.80	0.04	1.9	0.11	0.97	0.02	0.30	1.84	12.41	14.7	8.83	0.05	12.7	0.04
CaO	6.01	0.05	7.03	0.13	1.78	0.02	2.97	3.19	3.47	1.91	7.69	0.04	3.47	0.02
Na_2O	2.21	0.03	1.51	0.11	5.79	0.03	5.80	6.49	3.11	0.50	3.68	0.04	0.80	0.04
K_2O	8.84	0.05	1.81	0.08	5.41	0.03	4.74	4.16	0.37	0.28	0.35	0.02	0.23	0.01
P_2O_5			2.79	0.05	0.67	0.03	0.46	0.60	0.40	1.05	1.39	0.05	1.33	0.03
SO_3			0.29	0.13			0.07	0.06	0.26	0.96	0.17	0.02	0.63	0.02
Cl			0.34	0.05	0.11	0.01							0.33	0.01
Total	100.0		100.0		100.0		99.3	99.5	97.8	100.0	100.0		98.7	

[a] For these clasts, the bulk compositions were estimated using EPMA mineral compositions and their modal abundances (Table 3).
[b] 1σ is 1 sigma uncertainty based on counting statistics by the SEM-EDS software.

Table 3
Modalfraction of minerals in different Mn-bearing clasts, estimated using volume fractions from X-ray maps collected using the EPMA and approximated densities of minerals.

	weight fraction	Orthoclase	Albite	Pyroxenes	Plagioclase	Mn-rich region	Fe oxides	Apatite
Monzonite	7034 Js1b	0.26	0.67	0	0	0.01	0.05	0.01
Monzonite	7533 C2b	0.26	0.57	0.10	0	0.003	0.05	0.01
Clump	7034 1B, 3	0	0	0.36	0.42	0.09	0.01	0

Table 4
Estimated compositions of contamination-free Mn-oxides.

Molar ratios	Ranges from Fig. 8	Avg value	Moles/g of sample		Oxides[a]	wt%
Mn/Fe	2.5–2.8	2.6	Mn	0.746	MnO_2	64.8
Mg/Fe	0.2	0.20	Mg	0.057	MgO	2.29
Ca/Fe	0.4	0.40	Ca	0.115	CaO	6.42
Ba/Fe	0.03	0.03	Ba	0.009	BaO	1.32
K/Fe	0.04–0.05	0.04	K	0.011	K_2O	0.54
Na/Fe	0.11–0.13	0.12	Na	0.034	Na_2O	1.07
S/Fe	0.07	0.07	S	0.02	SO_3	1.61
P/Fe	0.13	0.08	P	0.034	P_2O_5	2.44
			Fe^{3+}[b]	0.251	Fe_2O_3	20.0
					Total	100.5

[a] Oxide contents were calculated assuming Mn is 4+ and Fe is 3+.
[b] Fe content was derived from Fig. 8b with a range from 12 to 16 wt%. We used 14 wt% to derived the rest of the element concentrations.

atmosphere, experiments showed that oxidation of Mn^{2+}(aq) is a slow process. The half-life of Mn^{2+}(aq) is ~400 days in a homogeneous solution with pH = 8 (Morgan, 2005), and within ~10–30 days at pH = 8 when oxide catalysts (e.g., Fe_2O_3 or ferrihydrite) are present (Morgan, 2005; Wang et al., 2015). Both Mn-rich regions in NWA 7034 and pairs and Mn-rich rocks on Mars contain high amounts of Fe, suggesting the presence of Fe-oxides or ferrihydrites that facilitated the oxidation of Mn^{2+}(aq). However, in contrast to the modern-day Earth atmosphere with a partial O_2 pressure (P_{O2}) of ~21,000 Pa, the present-day Martian atmosphere contains significantly less O_2 (P_{O2} = ~0.9 to 1.5 Pa, calculated from Mahaffy et al., 2013). Experimental studies of Mn oxidation rates under different partial O_2 pressures showed that oxidation of Mn^{2+}(aq) did not occur under purging N_2 in the same time scale as it does under air in the presence of the catalyst ferrihydrite (Wang et al., 2015). Therefore, if atmosphere conditions (pressure and composition) during formation of Mn-oxides were similar to modern-day Mars, the formation of Mn-oxides even with the presence of FeOOH and maghemite as catalysts will require the presence of a continuous, long-duration aqueous environment to compensate due to the slow kinetics of oxidation.

5. Conclusions

We present a detailed petrographical, mineralogical, and chemical report of Martian $Mn^{4+,3+}$-oxides in Mn-rich regions associated with different clasts in Martian regolith breccias NWA 7034 and 7533. The Martian origin of the $Mn^{4+,3+}$-oxides is established by the presence of Mn-rich glass domains (4.8–5.6 wt% Mn) in the fusion crust and the inclusion of high-valent Mn species within the glass. The Mn- K-edge XAS spectra of Mn-rich regions in monzonite clasts indicated that 67–85% of Mn is 4+ with the rest being 3+. Synchrotron XRD analysis of the Mn-rich region in the basalt clast also suggested that the Mn-mineral displays a cryptomelane structure, consistent with high valent Mn.

The $Mn^{4+,3+}$-oxides occur in Mn-rich regions as nanocrystalline grains mixed with silicates, FeOOH, and possible phosphates. These Mn-rich regions occur in diverse petrographic contexts in the studied samples, including common occurrences inside monzonite clasts and pyroxene clumps and less common occurrences inside two basalts, in contact with altered Fe-oxide fragment or with Fe-oxide as inclusions in an apatite grain, and in contact with an altered pyrite-pyrrhotite within a plagioclase fragment. Among the eight sections examined, Mn-rich regions are not present in the matrix of the breccias.

Mn-rich regions vary from 1 wt% to 34 wt% Mn, higher than the bulk Mn contents of these meteorites or those of included rock fragments. Based on the amount of mixing between FeOOH, pyroxenes, and Mn-oxides, the composition of the Mn-oxides is estimated to be ~39 wt% Mn, ~1.4 wt% Mg, ~2.9 wt% Ca, ~1.7 wt% Na, ~1.2 wt% Ba, 1.1 wt% P, and 0.6 wt% S. Enrichment of P and S in the Mn-rich glass relative to the regular glass in the fusion crust is consistent with the estimated Mn-oxide compositions. The estimated bulk compositions of Mn-oxide-bearing pyroxene clumps and the basalt clast are similar to the reported Mn-rich rocks from Opportunity and Curiosity rovers, suggesting a similar mixing of Mn-oxides with pyroxene and a small amount of feldspar in those field sites.

Given the absence of Mn-oxides in the matrix of NWA 7034 and 7533, the presence of Mn-oxides in different lithic and mineral clasts, the presence of Mn-oxides in pyroxene clumps but not in the matrix of breccias, and similar compositions between Mn-rich regions of different petrographic contexts, our results are most consistent with the formation of Mn-oxides after the formation of pyroxene clumps but before the formation of protobreccias, in a surface environment where different components were deposited in the sedimentary catchment. The chronology for NWA 7034 and 7533 indicates that the formation of Mn-oxides most likely took place between 4.4 and 1.35 Ga.

Significant deposits of Martian Mn-oxides require both enrichment of Mn by surface weathering of crustal rocks and subsequent precipitation from the surface fluid. Owing to the low overall abundance of Mn in the Martian crust (< 0.6 wt%), enrichment of Mn to >5 wt% requires a long-lasting fluid that will allow more abundant cations (e.g., Ca, Mg, Al, Fe) to be removed by precipitation. The oxidation of Mn^{2+}(aq) is a kinetically slow process even with FeOOH as a catalyst, especially given the current Martian atmosphere (~0.9 to 1.5 Pa O_2). Therefore, if the atmospheric/dissolved O_2 content was similar to modern-day Mars at the time of deposition, the formation of Mn-oxides would require the presence of a continuous, long-duration aqueous environment to compensate for the slow kinetics of oxidation. Together with findings of Mn-rich phases within Noachian and Hesperian sedimentary strata in Endeavour and Gale craters, our results suggest that Mn-oxides are a common weathering product on Mars surface. It may be a reasonable expectation that Mars 2020 mission will observe Mn-rich materials in the Jezero crater.

Declaration of Competing Interest

None.

Acknowledgements

A portion of this research was performed at the Jet Propulsion Laboratory (JPL), which is managed by the California Institute of Technology (Caltech) under the contract with NASA. We thank M. Newville and A. Lanzirotti at the Argonne National Laboratory for their assistance in synchrotron X-ray diffraction analysis and E. Stolper for providing NWA 7533 samples. An older version of the manuscript benefited greatly from critical reviews by two anonymous reviewers, E.B. Rampe, M. Humayun, and J. Catalano. We thank E.B. Rampe for handling this

manuscript and careful and constructive reviews by A. Udry and P. Gasda. YL thanks the support from the JPL-Caltech President's and Director's Fund. WWF acknowledges the support of the Simons Foundation Collaboration on the Origins of Life (SCOL), and UL a NSF Graduate Research Fellowship. Portions of the research were carried out at the Stanford Synchrotron Radiation Lightsource, SLAC National Accelerator Laboratory, which is supported by the U.S. Department of Energy, Office of Science, Office of Basic Energy Sciences. The SSRL Structural Molecular Biology Program is supported by the DOE Office of Biological and Environmental Research, and by the National Institutes of Health, National Institute of General Medical Sciences. Portions of this work were performed at HPCAT (Sector 16), Advanced Photon Source (APS), Argonne National Laboratory. HPCAT operations are supported by DOE-NNSA's Office of Experimental Sciences. The Advanced Photon Source is a U.S. Department of Energy (DOE) Office of Science User Facility operated for the DOE Office of Science by Argonne National Laboratory under Contract No. DE-AC02-06CH11357. The EPMA and SEM analyses were performed at the Caltech Geological and Planetary Science Division Analytical Facility, which was supported in part by NSF grants EAR-0318518 and DMR-00800065.

Appendix A. Supplementary data

Supplementary data to this article can be found online at https://doi.org/10.1016/j.icarus.2021.114471.

References

Agee, C.B., et al., 2013. Unique meteorite from early Amazonian Mars: water-rich basaltic breccia Northwest Africa 7034. Science 339, 780–785.
Al-Kathiri, A., Hofmann, B.A., Jull, A.J.T., Gnos, E., 2005. Weathering of meteorites from Oman: correlation of chemical and mineralogical weathering proxies with ^{14}C terrestrial ages and the influence of soil chemistry. Meteorit. Planet. Sci. 40, 1215–1239.
Anbar, A.D., Holland, H.D., 1992. The photochemistry of manganese and the origin of banded iron formations. Geochim. Cosmochim. Acta 56, 2595–2603.
Arvidson, R.E., et al., 2016. High concentrations of manganese and sulfur in deposits on Murray Ridge, Endeavour Crater, Mars. Am. Mineralog. 101, 1389–1405.
Baron, F., Gaudin, A., Lorand, J.-P., Mangold, N., 2019. New constraints on early Mars weathering conditions from an experimental approach on crust simulants. J. Geophys. Res. Planet. 124, 1783–1801.
Bellucci, J.J., Nemchin, A.A., Whitehouse, M.J., Humayun, M., Hewins, R., Zanda, B., 2015. Pb-isotopic evidence for an early, enriched crust on Mars. Earth Planet. Sci. Lett. 410, 34–41.
Berger, J.A., et al., 2019. Manganese enrichment pathways relevant to Gale Crater, Mars: evaporative concentration and chlorine-induced precipitation. In: Lunar and Planetary Science Conference, vol. 50, p. 2847.
Biagioni, C., Capalbo, C., Pasero, M., 2013. Nomenclature tunings in the hollandite supergroup. Eur. J. Mineral. 25, 85–90.
Bibring, J.-P., et al., 2006. Global mineralogical and aqueous Mars history derived from OMEGA/Mars express data. Science 312, 400–404.
Bland, P.A., Zolensky, M.E., Benedix, G.K., Sephton, M.A., 2006. Weathering of Chondritic Meteorites. In: Lauretta, D.S., McSween Jr., H.Y. (Eds.), Meteorites and the Early Solar System II. University of Arizona Press, Tucson, pp. 853–867.
Bouvier, L.C., et al., 2018. Evidence for extremely rapid magma ocean crystallization and crust formation on Mars. Nature 558, 586–589.
Bridges, J.C., Grady, M.M., 2000. Evaporite mineral assemblages in the nakhlite (martian) meteorites. Earth Planet. Sci. Lett. 176, 267–279.
Brown, G.M., Gu, B., 2006. The chemistry of perchlorate in the environment. In: Gu, B., Coates, J.D. (Eds.), Perchlorate. Springer, Boston, MA, pp. 17–47.
Chalmin, E., Farges, F., Brown, G.E., 2009. A pre-edge analysis of Mn K-edge XANES spectra to help determine the speciation of manganese in minerals and glasses. Contrib. Mineral. Petrol. 157, 111–126.
Crerar, D.A., Cormik, R.K., Barnes, H.L., 1980. Geochemistry of manganese: An overview. In: Varentsov, I.M., Gasselly, G. (Eds.), Geology and Geochemistry of Manganese, Vol. 1: General Problems: Mineralogy, Geochemistry, Methods. Stuttgart, Germany, pp. 293–394.
De Ferri, L., Arletti, R., Ponterini, G., Quartieri, S., 2011. XANES, UV-VIS and luminescence spectroscopic study of chromophores in ancient HIMT glass. Eur. J. Mineral. 23, 969–980.
Donovan, J.J., Tingle, T.N., 1996. An improved mean atomic number background correction for quantitative microanalysis. Microsc. Microanal. 2, 1–7.
Dorn, R.I., 2013. Rock coatings. In: Shroder, J., Pope, G.A. (Eds.), Treatise on Geomorphology. Academic Press, San Diego, CA, pp. 70–97.
Ehlmann, B.L., et al., 2011. Subsurface water and clay mineral formation during the early history of Mars. Nature 479, 53–60.
Gasda, P.J., et al., 2019. High-Mn sandstone as evidence for oxidized conditions in Gale crater lake. In: Lunar and Planetary Science Conference, vol. 50, p. 1620.
Glavin, D.P., et al., 2013. Evidence for perchlorates and the origin of chlorinated hydrocarbons detected by SAM at the Rocknest aeolian deposit in Gale crater. J. Geophys. Res. Planet. 118, 1955–1973.
Grotzinger, J.P., et al., 2015. Deposition, exhumation, and paleoclimate of an ancient lake deposit, Gale crater, Mars. Science 350. https://doi.org/10.1126/science.aac7575.
Guitreau, M., Flahaut, J., 2019. Record of low-temperature aqueous alteration of Martian zircon during the late Amazonian. Nat. Commun. 10, 2457.
Hammersley, A.P., Svensson, S.O., Hanfland, M., Fitch, A.N., Hausermann, D., 1996. Two-dimensional detector software: from real detector to idealised image or two-theta scan. High Pressure Res. 14, 235–248.
Haskin, L.A., et al., 2005. Water alteration of rocks and soils on Mars at the Spirit rover site in Gusev crater. Nature 436, 66–69.
Hecht, M.H., et al., 2009. Detection of perchlorate and the soluble chemistry of martian soil at the Phoenix lander site. Science 325, 64–67.
Hewins, R.H., et al., 2017. Regolith breccia Northwest Africa 7533: mineralogy and petrology with implications for early Mars. Meteorit. Planet. Sci. 52, 89–124.
Hogancamp, J.V., et al., 2018. Chlorate/Fe-bearing phase mixtures as a possible source of oxygen and chlorine detected by the sample analysis at Mars instrument in Gale crater, Mars. J. Geophys. Res. Planet. 123, 2920–2938.
Humayun, M., et al., 2013. Origin and age of the earliest Martian crust from meteorite NWA 7533. Nature 503, 513–516.
Hurowitz, J.A., McLennan, S.M., 2007. A ~3.5 Ga record of water-limited, acidic weathering conditions on Mars. Earth Planet. Sci. Lett. 260, 432–443.
Hurowitz, J.A., Fischer, W.W., Tosca, N.J., Milliken, R.E., 2010. Origin of acidic surface waters and the evolution of atmospheric chemistry on early Mars. Nat. Geosci. 3, 323–326.
Johnson, J.E., Webb, S.M., Thomas, K., Ono, S., Kirschvink, J.L., Fischer, W.W., 2013. Manganese-oxidizing photosynthesis before the rise of cyanobacteria. Proc. Natl. Acad. Sci. 110, 11238–11243.
Johnson, J.E., Webb, S.M., Ma, C., Fischer, W.W., 2016. Manganese mineralogy and diagenesis in the sedimentary rock record. Geochim. Cosmochim. Acta 173, 210–231.
Jull, A.J.T., 2006. Terrestrial ages of meteorites. In: Lauretta, D.S., McSween Jr., H.Y. (Eds.), Meteorites and the Early Solar System II. University of Arizona Press, Tucson, pp. 889–905.
Kounaves, S.P., et al., 2010. Wet chemistry experiments on the 2007 Phoenix Mars Scout Lander mission: data analysis and results. J. Geophys. Res. Planet. 115, E00E10.
Kounaves, S.P., Carrier, B.L., O'Neil, G.D., Stroble, S.T., Claire, M.W., 2014. Evidence of martian perchlorate, chlorate, and nitrate in Mars meteorite EETA79001: implications for oxidants and organics. Icarus 229, 206–213.
Kraus, W., Nolze, G., 1996. POWDER CELL - a program for the representation and manipulation of crystal structures and calculation of the resulting X-ray powder patterns. J. Appl. Crystallogr. 29, 301–303.
Krinsley, D., Dorn, R.I., DiGregorio, B., 2009. Astrobiological implications of rock varnish in Tibet. Astrobiology 9, 551–562.
Lanza, N.L., et al., 2014. High manganese concentrations in rocks at Gale crater, Mars. Geophys. Res. Lett. 41, 5755–5763.
Lanza, N.L., et al., 2016. Oxidation of manganese in an ancient aquifer, Kimberley formation, Gale crater, Mars. Geophys. Res. Lett. 43, 7398–7407.
Lasne, J., et al., 2016. Oxidants at the surface of Mars: a review in light of recent exploration results. Astrobiology 16, 977–996.
Leroux, H., et al., 2016. Exsolution and shock microstructures of igneous pyroxene clasts in the Northwest Africa 7533 Martian meteorite. Meteorit. Planet. Sci. 51, 932–945.
Liu, Y., et al., 2018. Diverse fluid activities on Mars: Zinc-bearing silicate and oxide in the Martian breccia meteorite Northwest Africa (NWA) 7533. In: Lunar and Planetary Science Conference, vol. 49, p. 1045.
Liu, Y., Ma, C., Beckett, J.R., Chen, Y., Guan, Y., 2016. Rare-earth-element minerals in martian breccia meteorites NWA 7034 and 7533: implications for fluid–rock interaction in the martian crust. Earth Planet. Sci. Lett. 451, 251–262.
Liu, Y., et al., 2017. Evidence for O_2-rich environments on mars from hydrous Mn(IV)-oxides in Northwest Africa (NWA) 7034 and 7533 meteorites. In: Lunar and Planetary Science Conference, vol. 48, p. 1345.
Lorand, J.-P., et al., 2015. Nickeliferous pyrite tracks pervasive hydrothermal alteration in Martian regolith breccia: a study in NWA 7533. Meteorit. Planet. Sci. 50, 2099–2120.
Lorand, J.-P., et al., 2020. The sulfur budget and sulfur isotopic composition of Martian regolith breccia NWA 7533. Meteorit. Planet. Sci. 55, 2097–2116.
Luo, Y., Tan, W., Suib, S.L., Qiu, G., Liu, F., 2018. Dissolution and phase transformation processes of hausmannite in acidic aqueous systems under anoxic conditions. Chem. Geol. 487, 54–62.
Ma, C., Beckett, J.R., Rossman, G.R., 2012. Browneite, MnS, a new sphalerite-group mineral from the Zakłodzie meteorite. Am. Mineral. 97, 2056–2059.
Ma, C., Tschauner, O., Bindi, L., Beckett, J.R., Xie, X., 2019. A vacancy-rich, partially inverted spinelloid silicate, $(Mg,Fe,Si)_2(Si,\square)O_4$, as a major matrix phase in shock melt veins of the Tenham and Suizhou L6 chondrites. Meteorit. Planet. Sci. 54, 1907–1918.
Mahaffy, P.R., et al., 2013. Abundance and isotopic composition of gases in the martian atmosphere from the curiosity rover. Science 341, 263–266.
McCubbin, F.M., et al., 2016. Geologic history of Martian regolith breccia Northwest Africa 7034: evidence for hydrothermal activity and lithologic diversity in the Martian crust. J. Geophys. Res. Planet. 121, 2120–2149.

Meslin, P.-Y., et al., 2018. Detection of hydrous manganese and iron oxides with variable phosphorus and magnesium contents in the lacustrine sediments of the Murray Formation, Gale, Mars. In: Lunar and Planetary Science Conference, vol. 49, p. 1447.
Mitra, K., Catalano, J.G., 2019. Chlorate as a potential oxidant on Mars: rates and products of dissolved Fe(II) oxidation. J. Geophys. Res. Planet. 124, 2893–2916.
Mittlefehldt, D.W., 1994. ALH84001, a cumulate orthopyroxenite member of the Martian meteorite clan. Meteoritics 29, 214–221.
Morgan, J.J., 2005. Kinetics of reaction between O_2 and Mn(II) species in aqueous solutions. Geochim. Cosmochim. Acta 69, 35–48.
Morris, R.V., et al., 2004. Mineralogy at Gusev crater from the Mössbauer spectrometer on the spirit rover. Science 305, 833–836.
Morris, R.V., et al., 2006. Mössbauer mineralogy of rock, soil, and dust at Meridiani Planum, Mars: opportunity's journey across sulfate-rich outcrop, basaltic sand and dust, and hematite lag deposits. J. Geophys. Res. Planet. 111. https://doi.org/10.1029/2006JE002791.
Muttik, N., et al., 2014. Inventory of H_2O in the ancient Martian regolith from Northwest Africa 7034: the important role of Fe oxides. Geophys. Res. Lett. 41, 8235–8244.
Nemchin, A.A., et al., 2014. Record of the ancient martian hydrosphere and atmosphere preserved in zircon from a martian meteorite. Nat. Geosci. 7, 638–642.
Noda, N., et al., 2019. Highly oxidizing aqueous environments on early Mars inferred from scavenging pattern of trace metals on manganese oxides. J. Geophys. Res. Planet. 124, 1282–1295.
Nyquist, L.E., et al., 2016. Rb-Sr and Sm-Nd isotopic and REE studies of igneous components in the bulk matrix domain of Martian breccia Northwest Africa 7034. Meteorit. Planet. Sci. 51, 483–498.
Parise, J.B., et al., 1998. Pressure dependence of hydrogen bonding in metal deuteroxides: a neutron powder diffraction study of $Mn(OD)_2$ and β-$Co(OD)_2$. Physics and Chemistry of Minerals 25, 130–137.
Post, J.E., 1999. Manganese oxide minerals: crystal structures and economic and environmental significance. Proc. Natl. Acad. Sci. 96, 3447–3454.
Post, J.E., Veblen, D.R., 1990. Crystal structure determinations of synthetic sodium, magnesium, and potassium birnessite using TEM and the Rietveld method. American Mineralogist 75, 477–489.
Putz, H., Schön, J.C., Jansen, M., 1999. Combined method for *ab initio* structure solution from powder diffraction data. J. Appl. Crystallogr. 32, 864–870.
Santos, A.R., et al., 2015. Petrology of igneous clasts in Northwest Africa 7034: implications for the petrologic diversity of the martian crust. Geochim. Cosmochim. Acta 157, 56–85.
Sautter, V., et al., 2016. Magmatic complexity on early Mars as seen through a combination of orbital, in-situ and meteorite data. Lithos. 254-255, 36–52.
Taylor, G.J., 2013. The bulk composition of Mars. Chemie der Erde - Geochemistry 72, 401–420.
Taylor, S.R., McLennan, S., 2008. Planetary Crusts: Their Composition, Origin and Evolution. Cambridge University Press, Cambridge.
Tebo, B.M., et al., 2004. Biogenic manganese oxides: properties and mechanisms of formation. Annu. Rev. Earth Planet. Sci. 32, 287–328.
Thaisen, K.G., Taylor, L.A., 2009. Meteorite fusion crust variability. Meteorit. Planet. Sci. 44, 871–878.
Velbel, M.A., 2014. Terrestrial weathering of ordinary chondrites in nature and continuing during laboratory storage and processing: review and implications for Hayabusa sample integrity. Meteorit. Planet. Sci. 49, 154–171.
Villalobos, M., Toner, B., Bargar, J., Sposito, G., 2003. Characterization of the manganese oxide produced by *pseudomo nas putida* strain MnB1. Geochim. Cosmochim. Acta 67, 2649–2662.
Wang, X., et al., 2015. The presence of ferrihydrite promotes abiotic formation of manganese (oxyhydr)oxides. Soil Sci. Soc. Am. J. 79, 1297–1305.
Ward, L.M., Stamenković, V., Hand, K., Fischer, W.W., 2019. Follow the oxygen: comparative histories of planetary oxygenation and opportunities for aerobic life. Astrobiology. 19, 811–824.
Webb, S.M., 2011. The microanalysis toolkit: X-ray fluorescence image processing software. AIP Conf. Proc. 1365, 196–199.
Webb, S.M., Tebo, B.M., Bargar, J.R., 2005. Structural characterization of biogenic Mn oxides produced in seawater by the marine *bacillus sp.* strain SG-1. Am. Mineral. 90, 1342–1357.
Whitney, D.L., Evans, B.W., 2010. Abbreviations for names of rock-forming minerals. Am. Mineral. 95, 185–187.
Wittmann, A., et al., 2015. Petrography and composition of Martian regolith breccia meteorite Northwest Africa 7475. Meteorit. Planet. Sci. 50, 326–352.
Xu, H., Chen, T., Konishi, H., 2010. HRTEM investigation of trilling todorokite and nano-phase Mn-oxides in manganese dendrites. Am. Mineral. 95, 556–562.
Yen, A.S., et al., 2005. An integrated view of the chemistry and mineralogy of martian soils. Nature 436, 49–54.
Zahnle, K., Haberle, R.M., Catling, D.C., Kasting, J.F., 2008. Photochemical instability of the ancient Martian atmosphere. J. Geophys. Res. Planet. 113. https://doi.org/10.1029/2008JE003160.
Ziegler, K., Sharp, Z.D., Agee, C.B., 2013. The unique NWA 7034 martian meteorite: evidence for multiple oxygen isotope reservoirs. In: Lunar and Planetary Science Conference, Vol. 44, p. 2639.